Multimode vibrational dynamics and orientational effects in fluorescence-encoded infrared spectroscopy. I. Response function theory

Lukas Whaley-Mayda,[1] Abhirup Guha,[1] and Andrei Tokmakoff[1, a)]

Department of Chemistry, James Franck Institute, and Institute for Biophysical Dynamics, The University of Chicago, Chicago, Illinois 60637, USA

(Dated: 13 October 2023)

Fluorescence-encoded infrared (FEIR) spectroscopy is an emerging technique for performing vibrational spectroscopy in solution with detection sensitivity down to single molecules. FEIR experiments use ultrashort pulses to excite a fluorescent molecule's vibrational and electronic transitions in a sequential, time-resolved manner, and are therefore sensitive to intervening vibrational dynamics on the ground state, vibronic coupling, and the relative orientation of vibrational and electronic transition dipole moments. This series of papers presents a theoretical treatment of FEIR spectroscopy that describes these phenomena and examines their manifestation in experimental data. This first paper develops a nonlinear response function description of Fourier-transform FEIR experiments for a two-level electronic system coupled to multiple vibrations, which is then applied to interpret experimental measurements in the second paper. Vibrational coherence between pairs of modes produce oscillatory features that interfere with the vibrations' population response in a manner dependent on the relative signs of their respective Franck-Condon wavefunction overlaps, leading to time-dependent distortions in FEIR spectra. The orientational response of population and coherence contributions are analyzed and the ability of polarization-dependent experiments to extract relative transition dipole angles is discussed. Overall, this work presents a framework for understanding the full spectroscopic information content of FEIR measurements to aid data interpretation and inform optimal experimental design.

[a)]Author to whom correspondence should be addressed: tokmakoff@uchicago.edu

I. INTRODUCTION

The development of ultrasensitive vibrational spectroscopy tools for single-molecule applications is a diverse area of research that has led to fundamental advances in chemistry, materials science, and molecular and optical physics. The experimental challenges posed by the weakness of molecular vibrations' light-matter interactions have been addressed in a variety of ways, and typically include either near-field enhancement by plasmonic effects, the coupling of the vibrations to more sensitive spectroscopic observables, or both.[1–7] Near-field approaches, such as surface- and tip-enhanced Raman methods, have been incredibly successful in single-molecule science, but are limited to investigations at metallic interfaces.[8,9] Recently, our group has developed fluorescence-encoded infrared (FEIR) spectroscopy as a strategy for single-molecule vibrational investigation in solution.[10] FEIR spectroscopy operates on fluorescent molecules and works by coupling their ground-state vibrational signals into fluorescence emission, which may then be detected with high sensitivity.

The principle of operation in an FEIR experiment can be described schematically by three sequential molecular steps: (1) excitation of a vibration by resonant IR absorption, (2) upconversion of the excited vibrational level to the electronic excited state by resonant visible absorption ('encoding'), and (3) emission of the fluorescence photon. The visible field used for encoding is tuned to be pre-resonant with the equilibrium electronic transition so that only the vibrationally excited molecules are selected, and steps (1) and (2) together (i.e. FEIR excitation) can be considered as a double-resonance pumping process. Underlying these steps are fast vibrational and electronic dynamics, making the overall process intrinsically time-dependent as well as nonlinear. Picosecond vibrational population relaxation ubiquitous in the condensed phase necessitates the use of short pulse excitation for steps (1) and (2) to ensure the overall process can be made sufficiently efficient. FEIR experiments with femtosecond pulses significantly shorter than these lifetimes are consequently directly sensitive to vibrational dynamics on the ground state prior to encoding. Furthermore, the encoding step is contingent on vibronic coupling between the probed vibrational coordinates and the electronic transition, and the nature of this coupling accordingly controls how vibrational signatures appear in FEIR signals. Additionally, the relative orientation of the transition dipole moments probed in steps (1) and (2) manifest experimentally in the polarization dependence of signals. Developing a detailed understanding of the molecular information content accessible in FEIR spectroscopy requires a theoretical treatment capable of properly cap-

turing these phenomena.

Our previous work on high sensitivity FEIR spectroscopy has largely explored the experimental principles for optimizing detection sensitivity toward single-molecule measurements.[10–12] Earlier work using instrumentation geared toward high concentration measurements and incorporating a two-photon encoding transition demonstrated how ultrafast vibrational dynamics, in particular multimode coherence, appear in FEIR signals, and explained these results within a simplified response function picture.[13,14] Building on this earlier analysis, here we develop a more comprehensive response function description of FEIR spectroscopy with one-photon encoding and use it to investigate the spectroscopic details of our current experimental implementation.

An important simplification in describing the overall FEIR process arises from the large separation of timescale between the femtosecond to picosecond vibrational dynamics and the nanosecond electronic relaxation involved in fluorescence emission. Namely, we can assume that the processes of FEIR excitation (steps (1) and (2)) and fluorescence emission (step (3)) are essentially independent. Our strategy is to describe the excitation process using the perturbative nonlinear response function formalism widely employed in multidimensional spectroscopy,[15,16] and then treat the emission process phenomenologically. This approach is characteristic of "action spectroscopy"—the class of techniques where the detected observable is an indirect read-out of the spectroscopic excitation, in contrast to conventional "coherent" methods that directly monitor absorption, scattering, interference, or amplification of the interrogating electromagnetic field and are described via the material polarization. Action observables are taken to be proportional to the population of an excited state or set of states that the system is driven into by the excitation method. Action techniques that detect fluorescence,[17–21] photocurrent,[22–27] photoelectrons,[28] and photoionization,[29–32] are gaining wider use in the field of multidimensional spectroscopy, and their formal relationship to conventional coherent spectroscopies in terms of response function theory—a system's coherent and action response corresponding at nonlinear orders n and $n+1$, respectively—has been well established.[33–37] This correspondence is exemplified in the link between coherent two-dimensional (2D) electronic spectroscopy, described by the nonlinear polarization to third order, and its fluorescence-detected counterpart, described by the excited population to fourth order.

Casting FEIR excitation in density matrix perturbation theory language requires developing the light-matter interaction to fourth order, as two perturbation-theoretic interactions each are required to describe the transfer of population in steps (1) and (2). In terms of nonlinear response,

FEIR spectroscopy is therefore on par with existing fourth-order action techniques, and by the correspondence discussed above also to third-order coherent techniques. We will use the resulting conceptual and technical analogies to our advantage by describing FEIR experiments in the well-developed language of these ultrafast nonlinear methods. Specifically, FEIR is a three-pulse (IR-IR-visible) experiment, in which the delay between two IR pulses generated by an interferometer (τ_{IR}) is scanned to resolve the vibrational excitation frequency via Fourier transformation, while the delay before the third pulse (τ_{enc}) acts as a waiting time in which the system evolves before the encoding step. These aspects of the experiment have direct analogies in 2D spectroscopy, although FEIR does not go on to resolve a second coherence period and conjugate frequency after the waiting time. As such, many direct similarities exist in the spectroscopic information content and how it is visualized, as well as in the practicalities of how measurements are conducted and data is processed. Mixed IR/visible techniques such as 2D vibrational-electronic (2D VE) spectroscopy and vibrationally promoted electronic resonance (VIPER) spectroscopy are especially closely related.[38–42]

While these analogies are useful, the primary motivations for developing FEIR spectroscopy—namely, for performing single-molecule experiments—are different from those of ultrafast and multidimensional spectroscopies and lead to different priorities in experimental design. For example, a more important goal would be to measure one-dimensional vibrational spectra with the highest possible detection sensitivity, while developing FEIR measurements that can probe ultrafast system dynamics or reveal the correlation between multiple transitions are of secondary importance. Nevertheless, this richness in spectroscopic information content is still important to understand, as it can have a major impact on the appearance of FEIR spectra and their interpretation.

Our analysis describes how FEIR measurements with broadband pulses contain contributions from two types of molecular response: single-mode population pathways involving individual vibrations, and multimode coherence pathways connecting pairs of coupled vibrations. The population response represents the sequential double-resonance pumping picture put forward initially and produces spectroscopically intuitive features—absorptive vibrational resonances with peak intensities that scale with the squares of the transition moments for the vibrational fundamental and vibronic encoding transitions, respectively, and decay away in τ_{enc} with the vibrational lifetime. On the other hand, coherence pathways arise from using broadband IR excitation pulses that cover multiple vibrational bands, and produce oscillatory signatures in τ_{enc} originating from the coherent

evolution of pairs of vibrational fundamentals. In FEIR spectra, these coherence pathways manifest as additional features overlapped on the population peaks that undergo τ_{enc}-dependent phase modulation and decay through coherence dephasing. The coherence amplitude is governed by a cyclic product of four transition dipoles that can have either positive or negative sign, resulting in either constructive or destructive interference against the population response at early τ_{enc}.

In terms of orientational response, the population pathways are governed by orientational correlation functions involving two unique dipoles, yielding polarization dependencies with anisotropy of the familiar second Legendre polynomial form common to many spectroscopic techniques that probe orientation.[43] FEIR anisotropy measurements performed by controlling the polarization angle between the IR and visible pulses can therefore be used to extract the relative orientation of the vibrational and vibronic encoding transitions in a molecule. However, coherence pathways have a more complicated orientational contribution—in the Condon approximation governed by three unique dipoles—which can also adopt a variable positive or negative sign. As we will demonstrate in Paper II, the combined effect of these possibilities in the vibronic and orientational response have a profound impact on the shape of FEIR spectra at early τ_{enc} before coherence has dephased.

This paper is organized as follows. Section II describes the fourth-order action response framework for calculating FEIR signals. Section III discusses the relationship between two useful experimental FEIR observables, spectra and two-pulse transients, and describes the phenomenology of population and coherence pathways in these measurements. Section IV analyzes the orientational response and discusses polarization-dependent measurements. Finally, Sec. V concludes Paper I and introduces Paper II.

II. FOURTH-ORDER ACTION DESCRIPTION OF FEIR SPECTROSCOPY

A. Model system

We consider a two-level electronic system consisting of a ground (g) and excited (e) state coupled to multiple vibrational coordinates. Owing to the resonance conditions and order of nonlinearity considered, on the electronic ground state only the singly-excited levels of the vibrations can be accessed in our description. Specifically, neither overtone nor combination states need to be considered, and FEIR measurements are consequently not directly sensitive to vibrational anharmonicity. We therefore adopt the level structure and notation shown in Figure 1(a), where

the ground electronic manifold is composed of the global ground state $|g,0\rangle = |g\rangle|0^g\rangle$ with zero quanta in all vibrational oscillators, and the set of singly-excited vibrational states $|g,1_i\rangle = |g\rangle|1_i^g\rangle$ in which the i-th mode has one quantum of excitation while all others remain in the ground state. The vibrational frequencies are assumed to be substantially higher than $k_BT/\hbar$ so that this one-quantum manifold is not appreciably populated at equilibrium. Similarly, the electronic excited manifold has the zero-quantum level $|e,0\rangle = |e\rangle|0^e\rangle$ and corresponding set of one-quantum levels $|e,1_i\rangle = |e\rangle|1_i^e\rangle$.

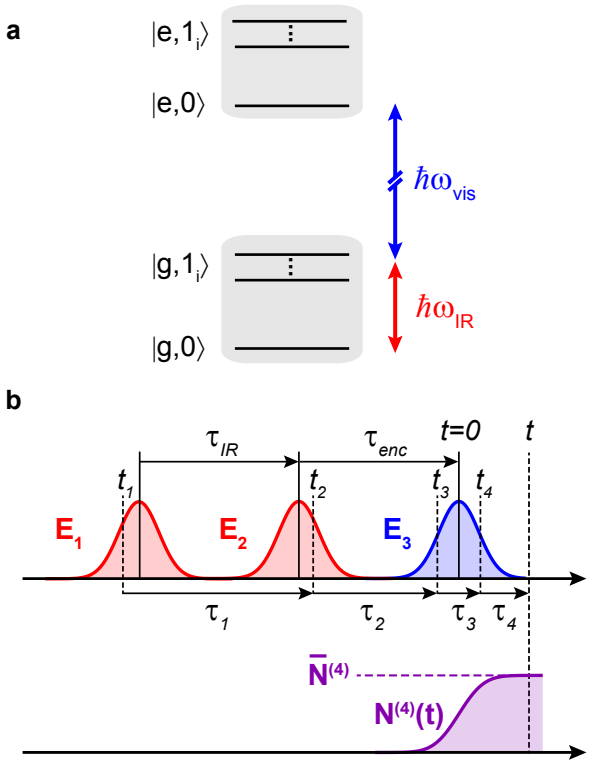

FIG. 1. Energy level diagram, pulse sequence, and target population in an FEIR experiment. (a) Generalized energy level diagram for FEIR excitation. Relative energy gaps are not to scale. (b) Pulse sequence (top), target excited population (bottom), and relevant time variables for the calculation of the system response.

The light-matter interaction taken in the electric dipole-approximation is

$$V(t) = -\mathbf{M}\cdot\mathbf{E}(t), \tag{1}$$

where $\mathbf{E}(t)$ is the incident electric field and $\mathbf{M}$ is the system dipole operator. A generic matrix element connecting system states a and b is given by

$$\langle b|\mathbf{M}|a\rangle = M_{ba}\hat{\mathbf{m}}_{ba}, \tag{2}$$

where M_{ba} is a scalar amplitude describing the strength of the transition dipole and $\hat{\mathbf{m}}_{ba}$ is a unit vector describing its orientation in the molecular frame. Specifically, to denote vibrational transition moments on the ground electronic state, e.g. $|a\rangle = |g,0\rangle$ and $|b\rangle = |g,1_i\rangle$, we use the notation $\mu_{i0}\hat{\boldsymbol{\mu}}_{i0}$.

Vibronic transitions between the electronic ground and excited manifolds are sensitive to vibrational-electronic coupling, which is correspondingly a critical molecular property required for FEIR signal generation. In the simplest case of no vibrational coordinate-dependence to the electronic transition moment (Condon approximation), the vibronic transition dipole moment factorizes,[40,44] e.g. for $|a\rangle = |g,1_i\rangle$ and $|b\rangle = |e,0\rangle$

$$\langle e,0|\mathbf{M}|g,1_i\rangle = \langle 0^e|1_i^g\rangle \mu_{eg}\hat{\boldsymbol{\mu}}_{eg}, \tag{3}$$

where μ_{eg} and $\hat{\boldsymbol{\mu}}_{eg}$ are the magnitude and orientation of the bare electronic transition, and $\langle 0^e|1_i^g\rangle$ is the vibrational wavefunction overlap, i.e. the Franck-Condon (FC) factor. We note that the term FC factor is sometimes used to refer to the square of the overlap integral, however in this work we use it to denote the overlap itself. Importantly, in the Condon approximation the orientation of the vibronic transitions are therefore aligned along $\hat{\boldsymbol{\mu}}_{eg}$.

The IR field (photon energy $\hbar\omega_{\mathrm{IR}}$ indicated by red arrow in Fig. 1(a)) is tuned to resonance with the vibrational fundamentals, and has sufficient bandwidth to cover multiple transitions. The visible encoding field (blue arrow) is tuned to be resonant with the transitions from $|g,1_i\rangle$ to $|e,0\rangle$. Importantly, the visible frequency ω_{vis} is below resonance with any transitions from the equilibrium ground state $|g,0\rangle$ to the electronic excited state, as otherwise direct one-photon absorption, e.g. creating excited electronic population to second-order in the light-matter interaction, would dominate. As a consequence of this resonance condition, transitions between the $|g,1_i\rangle$ and $|e,1_i\rangle$ manifolds are also out of resonance. Therefore, we only need to consider $|e,0\rangle$, and the higher vibrational levels can be ignored.

In general, the visible field should be made narrowband with respect to the electronic linewidth to ensure good spectral selectivity of double-resonance FEIR vs. one-photon excitation. The typical breadth of the electronic lineshape in solution, with associated inverse timescale of tens of femtoseconds, easily facilitates the selection of such a narrowband visible pulse (e.g. of a few hundred femtoseconds duration) that is still short compared to the picosecond vibrational lifetimes. Overall, optimizing the electronic pre-resonance condition is critical for successful measurements in practice, and has been investigated in Ref. 12.

B. Fluorescence signal

An action description assumes the spectroscopic signal is proportional to the population of a target excited state or set of states that the system is driven into by the incident electric fields. In our case we consider a single target state $|f\rangle = |e,0\rangle$, and calculate its population with the projection operator

$$A = |f\rangle\langle f|. \tag{4}$$

The pulse sequence used in an FEIR experiment is depicted in Fig. 1(b). Explicitly, the total incident electric field is

$$\mathbf{E}(t) = \mathbf{E}_1(t + \tau_{\text{enc}} + \tau_{\text{IR}}) + \mathbf{E}_2(t + \tau_{\text{enc}}) + \mathbf{E}_3(t), \tag{5}$$

where $\mathbf{E}_1$ and $\mathbf{E}_2$ are a pair of IR pulses separated by delay τ_{IR}, and $\mathbf{E}_3$ is the visible encoding pulse delayed with respect to $\mathbf{E}_2$ by the encoding delay τ_{enc}. These pulses propagate collinearly, and their parallel wave-vectors will therefore be left out of the notation. Two light-matter interactions with $\mathbf{E}_3$ are required to reach the target excited state, and barring cases of IR/Vis pulse overlap they must be directly sequential.

For well-separated pulses in the "proper" ordering shown in Fig. 1(b), the fourth-order contribution to the time-dependent target population $N(t)$ is

$$\begin{aligned} N^{(4)}(t) = \int_0^\infty d\tau_4 \int_0^\infty d\tau_3 \int_0^\infty d\tau_2 \int_0^\infty d\tau_1 \, \mathbf{R}^{(4)}(\tau_4,\tau_3,\tau_2,\tau_1) \\ \times \mathbf{E}_3(t-\tau_4)\mathbf{E}_3(t-\tau_4-\tau_3)\mathbf{E}_2(t-\tau_4-\tau_3-\tau_2+\tau_{\text{enc}}) \\ \times \mathbf{E}_1(t-\tau_4-\tau_3-\tau_2-\tau_1+\tau_{\text{enc}}+\tau_{\text{IR}}), \end{aligned} \tag{6}$$

where the multiplication of the fourth-rank tensorial response function $\mathbf{R}^{(4)}$ with the four field vectors is understood as a tensor contraction. The response function is

$$\begin{aligned} \mathbf{R}^{(4)}(\tau_4,\tau_3,\tau_2,\tau_1) = \\ \left(\frac{i}{\hbar}\right)^4 \theta(\tau_4)\theta(\tau_3)\theta(\tau_2)\theta(\tau_1)\text{Tr}\{A(\tau_4+\tau_3+\tau_2+\tau_1) \\ \times [\mathbf{M}(\tau_3+\tau_2+\tau_1),[\mathbf{M}(\tau_2+\tau_1),[\mathbf{M}(\tau_1),[\mathbf{M}(0),\rho_0]]]]\}, \end{aligned} \tag{7}$$

where ρ_0 is the equilibrium reduced system density operator, the τ_i are the time-delays between sequential interactions, $\theta(\tau_i)$ is the Heaviside step function, and $\text{Tr}\{\cdots\}$ denotes the trace.

Equation 6 describes the full time-evolution of the target population, which in principle could be made to include the radiative and nonradiative relaxation processes that lead to fluorescence emission and its quantum yield. However, the action approach aims to simply describe the signal by the final target population following the last light-matter interaction, with the quantum yield as a proportionality constant. In the impulsive limit where the electric field envelopes are much shorter than any system dynamics, this is accomplished straightforwardly by setting $\tau_4 = 0$. To develop a more general expression that works for finite duration pulses, we assume the relaxation timescale of the target state τ_f is much longer than the final pulse duration τ_p, and calculate the limiting target population $\bar{N}^{(4)}$ after the last pulse has finished interacting but before appreciable relaxation has set in, as is relevant for femtosecond excitation of strongly fluorescent molecules with excited-state lifetimes in the nanosecond range. Figure 1(b) depicts this limiting procedure. Specifically, we change variables to the absolute time of the last interaction $t_4 = t - \tau_4$, which modifies the final integration in Eq. 6 by $\int_0^\infty d\tau_4 \rightarrow \int_{-\infty}^t dt_4$. Because the target population's relaxation is assumed to be slow, A is approximately a constant of the motion under free system evolution so that $A(\tau_4 + \tau_3 + \tau_2 + \tau_1) \approx A$ in the response function (Eq. 7). Then the upper integration limit of the t_4 integral is safely extended to $t \rightarrow \infty$, as the product of the four electric fields will be essentially zero for these t_4 values. This also takes care of causality, so the step function $\theta(t - t_4)$ can be dropped from the response function. The result is

$$\begin{aligned}\bar{N}^{(4)} = \int_{-\infty}^{\infty} dt_4 \int_0^\infty d\tau_3 \int_0^\infty d\tau_2 \int_0^\infty d\tau_1 \, \mathbf{R}^{(4)}(\tau_3, \tau_2, \tau_1) \\ \times \mathbf{E}_3(t_4)\mathbf{E}_3(t_4 - \tau_3)\mathbf{E}_2(t_4 - \tau_3 - \tau_2 + \tau_{\text{enc}}) \\ \times \mathbf{E}_1(t_4 - \tau_3 - \tau_2 - \tau_1 + \tau_{\text{enc}} + \tau_{\text{IR}}),\end{aligned} \tag{8}$$

where the modified response function is

$$\begin{aligned}\mathbf{R}^{(4)}(\tau_3, \tau_2, \tau_1) = \left(\frac{i}{\hbar}\right)^4 \theta(\tau_3)\theta(\tau_2)\theta(\tau_1) \\ \times \text{Tr}\{A[\mathbf{M}(\tau_3 + \tau_2 + \tau_1), [\mathbf{M}(\tau_2 + \tau_1), \\ [\mathbf{M}(\tau_1), [\mathbf{M}(0), \rho_0]]]]\}.\end{aligned} \tag{9}$$

This effective action response function does not depend on τ_4, rather only on the time intervals between the four successive light-matter interactions, and from here on out we will exclusively work with this version of the response function.

Accounting for the fluorescence quantum yield ϕ, the average number of molecules in the observation volume $\langle n \rangle$, the overall detection efficiency of a fluorescence photon η, and the

repetition-rate of the experiment r, the average FEIR signal count rate from the sample is

$$F(\tau_{\mathrm{IR}},\tau_{\mathrm{enc}}) = r\eta\phi\langle n\rangle \bar{N}^{(4)}(\tau_{\mathrm{IR}},\tau_{\mathrm{enc}}), \tag{10}$$

where we have explicitly notated the dependence on the experimental inter-pulse delays implicit in Eq. 8. The total fluorescence count rate from the sample (excluding non-molecular background) is

$$F_{\mathrm{tot}}(\tau_{\mathrm{IR}},\tau_{\mathrm{enc}}) = F(\tau_{\mathrm{IR}},\tau_{\mathrm{enc}}) + F_0 \tag{11}$$

where F_0 is a background component due to direct one-photon visible excitation of the molecule (not described by Eq. 8).[12]

We will treat the effects of finite pulse durations, including different pulse interaction orderings that occur during their temporal overlap in Paper II. For the remainder of the current paper we will restrict our analysis to the impulsive limit.

C. Response function

The four nested commutators in the action response function (Eq. 9) produce $2^4 = 16$ Liouville pathways grouped into pairs, which represent 8 unique four-point dipole correlation functions and their complex conjugates. The formal correspondence between pathways in fourth-order action and third-order coherent response has been discussed extensively in the context of fluorescence-detected 2D electronic spectroscopy.[33–36,45] The resonance conditions of FEIR spectroscopy impose constraints that greatly reduce the number of pathways that need to be considered. Specifically, because the target state is only accessible through two-photon material resonances involving the singly-excited vibrational states as intermediates (Fig. 1(a)), two bra- and ket-side interactions each are required per pathway. This condition is only satisfied by 3 out of the 8 correlation functions, which we take to constitute the response function as follows

$$\mathbf{R}^{(4)}(\tau_3,\tau_2,\tau_1) = \frac{1}{\hbar^4}\theta(t_3)\theta(\tau_2)\theta(\tau_3)\sum_{\alpha=1}^{3}\left[\mathbf{C}_\alpha(\tau_3,\tau_2,\tau_1) + \mathbf{C}_\alpha(\tau_3,\tau_2,\tau_1)^*\right] \tag{12a}$$

where

$$\mathbf{C}_1(\tau_3,\tau_2,\tau_1) =$$
$$\mathrm{Tr}\{A\mathbf{M}(\tau_2+\tau_1)\mathbf{M}(0)\rho_0\mathbf{M}(\tau_1)\mathbf{M}(\tau_3+\tau_2+\tau_1)\} \tag{12b}$$
$$\mathbf{C}_2(\tau_3,\tau_2,\tau_1) =$$
$$\mathrm{Tr}\{A\mathbf{M}(\tau_3+\tau_2+\tau_1)\mathbf{M}(0)\rho_0\mathbf{M}(\tau_1)\mathbf{M}(\tau_2+\tau_1)\} \tag{12c}$$
$$\mathbf{C}_3(\tau_3,\tau_2,\tau_1) =$$
$$\mathrm{Tr}\{A\mathbf{M}(\tau_1)\mathbf{M}(0)\rho_0\mathbf{M}(\tau_2+\tau_1)\mathbf{M}(\tau_3+\tau_2+\tau_1)\}. \tag{12d}$$

These three correlation functions also represent the subset of fourth-order pathways relevant for two-photon absorption spectroscopies.[46,47] We note that $\mathbf{R}^{(4)}$ is proportional to the real parts of its constituent correlation functions (i.e. complex conjugate terms are summed), which is a general feature of the even-order, while odd-order response functions instead depend on the imaginary parts of the dipole correlation functions.[15,45]

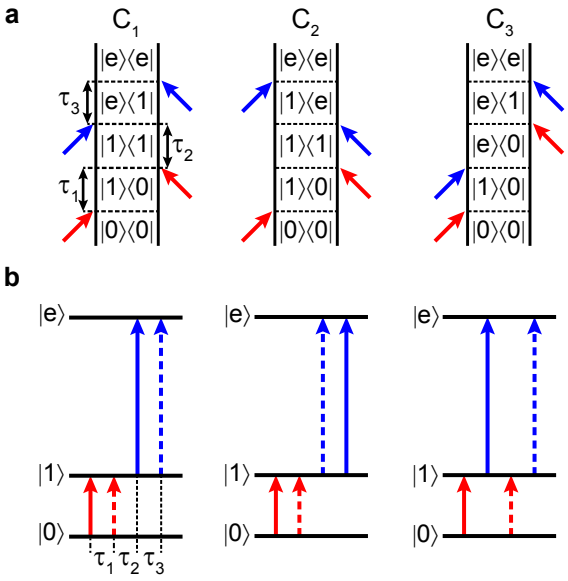

FIG. 2. (a) Double-sided Feynman diagrams and (b) ladder diagrams for the unique pathway contributing to each correlation function C_1, C_2, and C_3 in the case of a single vibration coupled to the electronic transition. Red and blue arrows indicate IR and visible field interactions, respectively. C_3 pathways do not contribute to FEIR signals under typical experimental conditions and can be neglected.

Assuming that the system's vibronic and rotational dynamics are independent,[48,49] the correlation functions can be factorized when expanded over system eigenstates indexed by a, b, c, and d

as

$$(C_\alpha)_{IJKL}(\tau_3,\tau_2,\tau_1) = \sum_{a,b,c,d} C_\alpha^{a,b,c,d}(\tau_3,\tau_2,\tau_1)(Y_\alpha)_{IJKL}^{a,b,c,d}(\tau_3,\tau_2,\tau_1), \tag{13}$$

where $C_\alpha^{a,b,c,d}$ are scalar pathways describing the system's vibronic response, while $(Y_\alpha)_{IJKL}^{a,b,c,d}$ make up the tensorial orientational correlation functions with I,J,K and L each indexing the laboratory-frame Cartesian coordinates X,Y, and Z. These orientational pathways will be treated in Sec. IV, and the remainder of this section and Sec. III will discuss the vibronic response only.

In the homogeneous limit, i.e. adopting independent optical Bloch propagators for each time interval, the scalar vibronic pathways are

$$\begin{aligned} C_1^{a,b,c,d}(\tau_3,\tau_2,\tau_1) =& \delta_{fc}M_{dc}M_{cb}M_{ad}M_{ba}P(a) \\ &\times \exp\left(-i\omega_{cd}\tau_3 - i\omega_{bd}\tau_2 - i\omega_{ba}\tau_1\right) \\ &\times \exp\left(-\Gamma_{cd}\tau_3 - \Gamma_{bd}\tau_2 - \Gamma_{ba}\tau_1\right) \end{aligned} \tag{14a}$$

$$\begin{aligned} C_2^{a,b,c,d}(\tau_3,\tau_2,\tau_1) =& \delta_{fc}M_{cb}M_{dc}M_{ad}M_{ba}P(a) \\ &\times \exp\left(-i\omega_{bc}\tau_3 - i\omega_{bd}\tau_2 - i\omega_{ba}\tau_1\right) \\ &\times \exp\left(-\Gamma_{bc}\tau_3 - \Gamma_{bd}\tau_2 - \Gamma_{ba}\tau_1\right) \end{aligned} \tag{14b}$$

$$\begin{aligned} C_3^{a,b,c,d}(\tau_3,\tau_2,\tau_1) =& \delta_{fc}M_{dc}M_{ad}M_{cb}M_{ba}P(a) \\ &\times \exp\left(-i\omega_{cd}\tau_3 - i\omega_{ca}\tau_2 - i\omega_{ba}\tau_1\right) \\ &\times \exp\left(-\Gamma_{cd}\tau_3 - \Gamma_{ca}\tau_2 - \Gamma_{ba}\tau_1\right). \end{aligned} \tag{14c}$$

Here $\omega_{ij} = (E_i - E_j)/\hbar$ are system eigenfrequencies, Γ_{ij} is a population relaxation rate for $i = j$ and a dephasing rate for $i \neq j$, $P(a)$ is the equilibrium population of the initial state a, and the Kroenecker delta δ_{fi} is the effect of the projection operator A (Eq. 4) ensuring the final state in the pathway is the target state $|f\rangle$.

Figure 2 shows double-sided Feynman and ladder diagrams for these pathways for a three-level system (discussed in Sec. III B). In the conventional language of ultrafast and multidimensional spectroscopy, pathways belonging to C_1 and C_2 represent excited-state absorption, while C_3 pathways represent double quantum coherence. C_1 and C_2 have non-rephasing and rephasing character, respectively, although this distinction does not produce important spectroscopic consequences as the τ_3 interval is not experimentally resolved (discussed further in Sec. III B). In each case, all

four interactions are absorptive and the pathway carries an overall positive sign due to having two bra-side interactions, thereby contributing a gain in fluorescence output from the molecule. These qualities are precisely those we selected for when invoking the resonance conditions to restrict the number of correlation functions under consideration—ground-state bleaching or stimulated emission pathways consequently do not contribute. Under these conditions we may therefore consider $\bar{N}^{(4)}$ as representing an overall FEIR excitation probability, as discussed heuristically in Ref. 12.

We note that alternative resonance conditions could in principle be used where these assumptions no longer hold. For example, in Ref. 13 a "fluorescence-loss" resonance condition was demonstrated in which the encoding field was tuned to be maximally resonant with the equilibrium electronic transition (in that case, a two-photon resonance), resulting in a negative-going FEIR signal (i.e. a decrease in total fluorescence relative to F_0 in Eq. 11). Within that resonance condition bleaching pathways dominate and a different subset of the 8 fourth-order correlation functions would need to be considered.

III. SINGLE-MODE AND MULTIMODE PATHWAYS IN FEIR SIGNALS

A. Two- and three-pulse signals and FEIR spectra

The full pulse sequence shown in Fig. 1(b) facilitates the measurement of Fourier transform (FT) vibrational spectra as a function of encoding delay τ_{enc}. The total FEIR signal is the sum of the following three contributions

$$F(\tau_{\text{IR}}, \tau_{\text{enc}}) = F_{12}(\tau_{\text{IR}}, \tau_{\text{enc}}) + F_1(\tau_{\text{IR}} + \tau_{\text{enc}}) + F_2(\tau_{\text{enc}}), \tag{15}$$

where we have suppressed the dependence on pulse polarization (discussed later in Sec. IV). The contribution F_{12}, termed the three-pulse signal, is due to one interaction each with $\mathbf{E}_1$ and $\mathbf{E}_2$ and two with the encoding field $\mathbf{E}_3$. Equation 8 explicitly calculates only this three-pulse contribution to $\bar{N}^{(4)}$. The three-pulse signal resolves the vibrational free-induction decay in τ_{IR} and is consequently the desired signal for measuring vibrational spectra. The contributions F_1 and F_2 are two-pulse signals where both IR-vibrational interactions occur with either $\mathbf{E}_1$ or $\mathbf{E}_2$, respectively, and can be found from Eq. 8 by modifying the product of the four pulse electric fields accordingly. The coexistence of these signal components is analogous to 2D spectroscopy experiments performed in the pump-probe geometry, where the 2D signal (analogous to F_{12}) must be separated from the pump-probe signals (analogous to F_1 and F_2).[50–53]

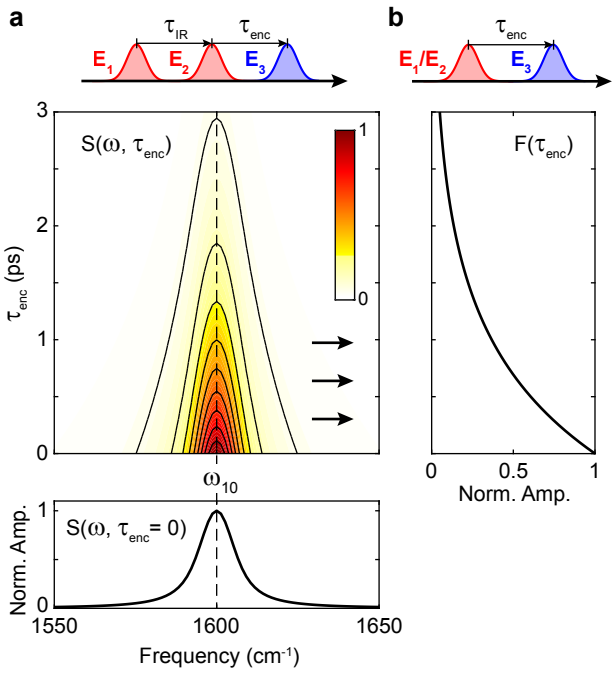

FIG. 3. Projection-slice relationship between (a) the FEIR spectrum $S(\omega, \tau_{\mathrm{enc}})$ derived from the three-pulse signal and (b) the two-pulse signal $F(\tau_{\mathrm{enc}})$. Results are shown for a single lifetime-broadened vibrational mode at ω_{10} = 1600 cm^{-1} with $\Gamma_{11}^{-1} = \Gamma_{10}^{-1}$ = 1 ps calculated in the impulsive limit. Panel (b) shares the same y axis as the top panel in (a), and both top and bottom panels in (a) share a common x axis.

By symmetry, the two- and three-pulse signals are related via

$$F_{12}(\tau_{\mathrm{IR}} = 0, \tau_{\mathrm{enc}}) \propto F_1(\tau_{\mathrm{enc}}) = F_2(\tau_{\mathrm{enc}}). \tag{16}$$

The FEIR spectrum, shown in Fig. 3(a), is given by the real part of the one-sided FT of the three-pulse signal

$$S(\omega, \tau_{\mathrm{enc}}) = \mathrm{Re} \int_0^{\infty} F_{12}(\tau_{\mathrm{IR}}, \tau_{\mathrm{enc}}) e^{i\omega\tau_{\mathrm{IR}}} d\tau_{\mathrm{IR}}. \tag{17}$$

The two-pulse signal (Fig. 3(b)) measures the τ_{enc}-dependence of the integrated vibrational resonances projected onto the τ_{enc} axis, as described formally by the projection-slice theorem

$$F_{12}(\tau_{\mathrm{IR}} = 0, \tau_{\mathrm{enc}}) = \int_{-\infty}^{\infty} S(\omega, \tau_{\mathrm{enc}}) d\omega \tag{18}$$

in conjunction with Eq. 16. Along the same lines, this relationship between the FEIR spectrum and two-pulse signal is directly analogous to that between the absorptive 2D spectrum and dispersed pump-probe signal.

In practice, the two-pulse signal can be measured either by blocking $\mathbf{E}_1$ (measuring $F_2(\tau_{\text{enc}})$), or setting $\tau_{\text{IR}} = 0$ (measuring $F_{12}(\tau_{\text{IR}} = 0, \tau_{\text{enc}}) + F_1(\tau_{\text{enc}}) + F_2(\tau_{\text{enc}})$). Due to the effect of constructive interference, this latter method produces a 4 times larger signal size than the former, as will be demonstrated experimentally in Paper II. For brevity, we will refer to the two-pulse signal simply by $F(\tau_{\text{enc}})$.

B. Single-mode population response

The primary molecular response interrogated in FEIR spectroscopy is due to the excitation and encoding of individual vibrational modes. In these single-mode pathways, both IR light-matter interactions occur with the same vibrational transition, and consequently both visible interactions also occur with the same vibronic transition. To describe the contribution of these single-mode pathways we therefore consider the simplest case of a single vibrational oscillator coupled to the electronic transition. Simplifying the notation in Fig. 1(a), this case is represented by a three-level system consisting of the global ground state $|0\rangle \equiv |g,0\rangle$, first vibrational excited state $|1\rangle \equiv |g,1\rangle$, and zero-quantum level of the excited electronic state $|e\rangle \equiv |e,0\rangle$ which is the target state. This model produces one unique material pathway per correlation function, which are shown in Fig. 2 as both double-sided Feynman diagrams and ladder diagrams. Filling in the eigenstate indices according to Eq. 14, the single-mode pathways $C_1^{0,1,e,1}$ and $C_2^{0,1,e,1}$ will be referred to as population pathways, as they report on the excited population of the vibration being pumped.

In the homogeneous limit the population pathways have the form

$$C_1^{0,1,e,1} = |\mu_{eg}|^2 \langle 0^e|1^g\rangle^2 |\mu_{10}|^2 \exp\Big[\big(-i(\omega_{e0}-\omega_{10}) - \Gamma_{e1}\big)\tau_3 - \Gamma_{11}\tau_2 + (-i\omega_{10} - \Gamma_{10})\tau_1\Big] \tag{19a}$$

$$C_2^{0,1,e,1} = |\mu_{eg}|^2 \langle 0^e|1^g\rangle^2 |\mu_{10}|^2 \exp\Big[\big(i(\omega_{e0}-\omega_{10}) - \Gamma_{e1}\big)\tau_3 - \Gamma_{11}\tau_2 + (-i\omega_{10} - \Gamma_{10})\tau_1\Big]. \tag{19b}$$

The τ_1- and τ_3-dependence describe the frequency and linewidth of the vibrational and vibronic transitions, respectively, while vibrational population relaxation during τ_2 causes the response to decay and represents a loss channel for the overall FEIR excitation probability. Because the squared electronic transition matrix element $|\mu_{eg}|^2$ will always be present in any pathway's amplitude, we will call the product $\langle 0^e|1^g\rangle^2 |\mu_{10}|^2$ the (Condon approximation) FEIR activity of the vibration. Within a given molecule, the FEIR activity is a simple indicator of the strength of

a vibration's FEIR response, although orientational factors also contribute (Sec. IV). For a displaced harmonic oscillator model which characterizes vibronic coupling by the Huang-Rhys factor $S = d^2/2$ where d is the dimensionless displacement between the ground and excited nuclear potentials, the squared FC factor is $\langle 0^e|1^g\rangle^2 = S\exp(-S) \approx S$ where the last approximation holds for small S. In this case, the FEIR activity is succinctly given by $S|\mu_{10}|^2$. In some systems, notably those where symmetry constraints cause FC factors to vanish, non-Condon effects could also play a role in FEIR activity which would require a more general description of the vibronic transition moment M_{e1}.[40,54,55]

While the C_3 pathway satisfies the resonance conditions, it involves the mixed IR-Vis-IR-Vis ordering of light-matter interactions, and therefore can only contribute during the temporal overlap of the IR and visible fields, i.e. when $|\tau_{\text{enc}}| \lesssim \tau_p$, where τ_p is the longest pulse duration. Explicitly,

$$\begin{aligned} C_3^{0,1,e,1} = |\mu_{eg}|^2\langle 0^e|1^g\rangle^2|\mu_{10}|^2 \exp\Big[&\big(-i(\omega_{e0}-\omega_{10})-\Gamma_{e1}\big)\tau_3 \\ &+\big(-i\omega_{e0}-\Gamma_{e0}\big)\tau_2+(-i\omega_{10}-\Gamma_{10})\tau_1\Big]. \end{aligned} \tag{20}$$

This pathway involves a rapidly oscillating electronic coherence $|e\rangle\langle 0|$ during τ_2 which typically dephases within tens of femtoseconds, and will not contribute to the signal with the pulse durations used in our experiments. Specifically, we will show in Paper II that C_3 pathways do not survive the finite-pulse convolution integrals in simulations, and can be safely neglected.

In the impulsive limit, the τ_1-dependence is mapped out in the IR pulse-pair delay τ_{IR}, τ_2 becomes the encoding delay τ_{enc}, and $\tau_3 = 0$ as the two interactions with $\mathbf{E}_3$ become time-coincident. Similarly, $C_3 \propto \delta(\tau_{\text{enc}})$ and therefore vanishes for positive τ_{enc} and will be ignored. Explicitly, the three-pulse signal is

$$\begin{aligned} &F_{12}(\tau_{\text{IR}},\tau_{\text{enc}}) \sim \\ &\quad \theta(\tau_{\text{enc}})\theta(\tau_{\text{IR}})\Big[C_1(0,\tau_{\text{enc}},\tau_{\text{IR}})+C_2(0,\tau_{\text{enc}},\tau_{\text{IR}})+c.c.\Big] \\ &\quad = \theta(\tau_{\text{enc}})\theta(\tau_{\text{IR}})4|\mu_{eg}|^2\langle 0^e|1^g\rangle^2|\mu_{10}|^2\exp(-\Gamma_{11}\tau_{\text{enc}}) \\ &\qquad\qquad \times\cos(\omega_{10}\tau_{\text{IR}})\exp(-\Gamma_{10}\tau_{\text{IR}}). \end{aligned} \tag{21}$$

The resulting FEIR spectrum ($\omega > 0$) is

$$\begin{aligned} &S(\omega,\tau_{\text{enc}}) \sim \\ &\quad \theta(\tau_{\text{enc}})|\mu_{eg}|^2\langle 0^e|1^g\rangle^2|\mu_{10}|^2\frac{\Gamma_{10}\exp(-\Gamma_{11}\tau_{\text{enc}})}{(\omega-\omega_{10})^2+\Gamma_{10}^2}, \end{aligned} \tag{22}$$

which is shown in Fig. 3(a). The spectrum resolves the vibrational fundamental's frequency and lineshape in an identical manner to a conventional linear IR absorption spectrum, and decays in τ_{enc} due to vibrational population relaxation. The two-pulse signal

$$\begin{aligned} F(\tau_{\mathrm{enc}}) &\sim \theta(\tau_{\mathrm{enc}})\Big[C_1(0,\tau_{\mathrm{enc}},0)+C_2(0,\tau_{\mathrm{enc}},0)+c.c.\Big] \\ &= \theta(\tau_{\mathrm{enc}})4|\mu_{eg}|^2\langle 0^e|1^g\rangle^2|\mu_{10}|^2\exp(-\Gamma_{11}\tau_{\mathrm{enc}}) \end{aligned} \tag{23}$$

correspondingly tracks this relaxation directly without resolving the lineshape via the projection-slice relationship (Fig. 3(b)).

The C_1 and C_2 pathways differ only in the sign of their τ_3 phase evolution. The C_1 pathway has the same sign of phase evolution during τ_1 and τ_3 and can therefore be classified as a non-rephasing pathway, while the C_2 pathway exhibits opposite signs and is consequently a rephasing pathway. The presence of correlated heterogeneity between the vibrational and electronic transition frequencies will therefore affect these pathways differently, although the large mismatch in magnitude of these frequencies precludes strong echo behavior.[56] Furthermore, because both the third and fourth light-matter interaction occur with the same pulse, the phase evolution in τ_3 is not directly monitored. These pathways are therefore not distinguishable in experiment, and contribute similarly to the measured signals. FEIR spectroscopy is consequently not directly sensitive to heterogeneity in the way that the related non-degenerate third-order technique 2D VE is.[38,39] The rephasing/non-rephasing terminology is however still useful for bookkeeping purposes when setting up finite-pulse calculations in Paper II.

C. Multimode coherence

1. Coherence pathway pairs

When multiple vibrational modes are covered within the bandwidth of the IR pulses, pairs of fundamentals may be excited coherently if the vibrations are coupled. A system of k modes will therefore in general produce $k!/(2!(k-2)!)$ coherences connecting all pairs of modes. To describe the phenomenology of these coherent signals, we consider a two-mode system resulting in four levels: the ground state $|0\rangle$, singly-excited vibrational states $|m\rangle \equiv |g,1_m\rangle$ and $|n\rangle \equiv |g,1_n\rangle$, and the target excited state $|e\rangle$. In addition to the population pathways residing in either $|m\rangle\langle m|$ or $|n\rangle\langle n|$ during τ_2 described above, there is the possibility for pathways residing in an $|m\rangle\langle n|$ or

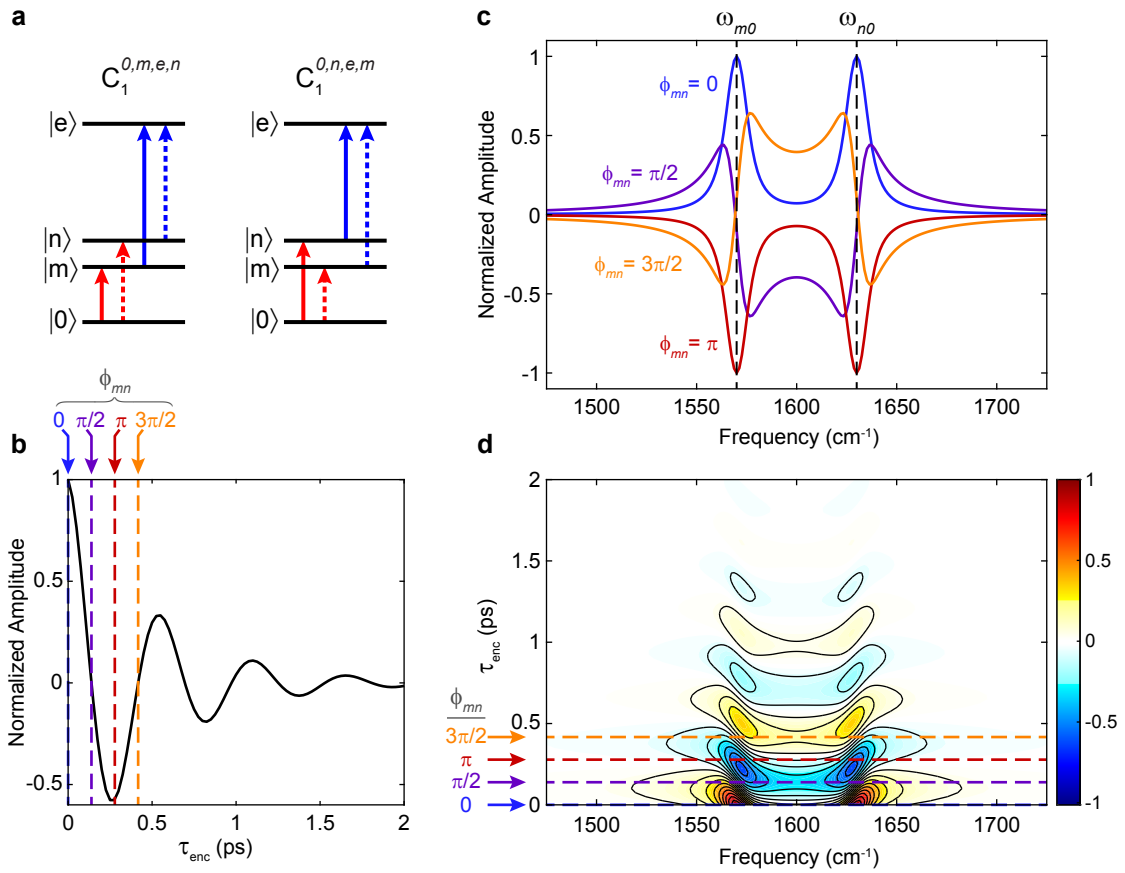

FIG. 4. Vibrational coherence pathways and their τ_{enc}-dependent signatures. (a) Ladder diagrams for the pair of C_1 coherence pathways connecting fundamentals m and n. (b) Isolated contribution of the coherence pair $(C_1^{0,m,e,n}+C_1^{0,n,e,m}+C_2^{0,m,e,n}+C_2^{0,n,e,m}+c.c.)$ to the impulsive two-pulse signal. The fundamentals have frequencies ω_{m0} = 1570 cm^{-1} and ω_{n0} = 1630 cm^{-1}, are lifetime-broadened with $\Gamma_{mm}^{-1}=\Gamma_{nn}^{-1}=\Gamma_{m0}^{-1}=\Gamma_{n0}^{-1}=$ 1000 fs, and the coherence dephasing is $\Gamma_{nm}^{-1}=500$ fs. (c) Lineshapes of the coherence pair contribution to the FEIR spectrum after acquiring phases of $\phi_{mn}=0,\pi/2,\pi$, and $3\pi/2$ through τ_{enc}-evolution (dephasing removed to better demonstrate the cycle of phase). (d) Contribution of the coherence pair to the impulsive τ_{enc}-dependent FEIR spectrum, with $\Gamma_{nm}^{-1}=500$ fs. Color-coded dashed lines in (b) and (d) indicate the τ_{enc} values corresponding to the different coherence phases in (c).

$|n\rangle\langle m|$ coherence during τ_2. Specifically, each correlation function has a matched pair of coherence pathways formed by exchanging the roles of the two vibrations m and n, i.e. that differ by which mode is excited first. Such a pair of pathways is shown for C_1 in Fig. 4(a), while the analogous pair for C_2 would be found by switching the order of the final two interactions with the visible

field. Explicitly, this pair of pathways has the form

$$\begin{aligned} C_1^{0,m,e,n} &= M_{en}^* M_{em} M_{n0}^* M_{m0} \\ &\quad \times \exp\Big[(-i(\omega_{eg}-\omega_{n0})-\Gamma_{en})\tau_3 \\ &\quad + (-i\omega_{mn}-\Gamma_{mn})\tau_2 + (-i\omega_{m0}-\Gamma_{m0})\tau_1\Big], \end{aligned} \tag{24a}$$

$$\begin{aligned} C_1^{0,n,e,m} &= M_{em}^* M_{en} M_{m0}^* M_{n0} \\ &\quad \times \exp\Big[(-i(\omega_{eg}-\omega_{m0})-\Gamma_{em})\tau_3 \\ &\quad + (-i\omega_{nm}-\Gamma_{nm})\tau_2 + (-i\omega_{n0}-\Gamma_{n0})\tau_1\Big]. \end{aligned} \tag{24b}$$

As the C_1 and C_2 pathways contribute identically to the FEIR signal, we will refer to the sum $C_1^{0,m,e,n} + C_1^{0,n,e,m} + C_2^{0,m,e,n} + C_2^{0,n,e,m} + c.c.$ as the coherence contribution to the signal, or coherence pathway pair, from the two vibrations.

2. Coherence oscillation and lineshape

The pair of coherence pathways exhibit oscillatory behavior in τ_2 at the difference frequency $|\omega_{mn}|$ between the vibrational fundamentals. In the two-pulse signal, shown in Fig. 4(b), the coherence pair manifests as an oscillatory signal damped by the coherence dephasing rate Γ_{mn}. In the FEIR spectrum, the oscillating part of the τ_2-dependence acts as a phase-shift (i.e. $\phi_{mn}(\tau_2) = \omega_{mn}\tau_2$ in Eq. 24(a)) on the vibrational lineshape encoded in the pathway's τ_1-dependence. This phase has opposite sign for the two members of the coherence pair, $\phi_{mn}(\tau_2) = -\phi_{nm}(\tau_2)$. The resulting contribution of the coherence to the spectrum is shown in Fig. 4(c), with the dephasing $\Gamma_{nm} = \Gamma_{mn} = 0$ for purposes of illustration. At $\tau_2 = 0$ the coherence phase is zero, and $C_1^{0,m,e,n}$ and $C_1^{0,n,e,m}$ produce absorptive vibrational lineshapes centered at ω_{m0} and ω_{n0}, respectively. As τ_2 increases, the phase evolves with opposite signs over each resonance, leading to dispersive lineshapes with overlapping negative lobes at $\phi_{mn} = -\phi_{nm} = \pi/2$, inverted absorptive lineshapes at $\phi_{mn} = -\phi_{nm} = \pi$, and then dispersive lineshapes with overlapping positive lobes at $\phi_{mn} = -\phi_{nm} = 3\pi/2$. We note that the sign of phase evolution is fixed by the frequency ordering of the modes, i.e. the lower lying resonance (ω_{m0} in Fig. 4) always acquires positive phase $\phi_{mn} > 0$ while the higher lying resonance (ω_{n0}) acquires negative phase $\phi_{nm} < 0$. Represented as an $(\omega, \tau_{\text{enc}})$ surface (Fig. 4(d)), the nodal lines over each resonance are therefore always "tilted away" from each other. This cyclic phase-twisting behavior is reminiscent of certain phase modulation effects in 2D peak

lineshapes caused by multilevel coherence during the waiting time,[16,57] although the involvement of a larger number of pathways and the distinction between rephasing and non-rephasing character make the behavior and its explanation more complicated in the latter case.

The coherence dephasing rate Γ_{nm} has contributions from both energy relaxation (i.e. the concomitant decay of the excited $|m\rangle$ and $|n\rangle$ populations) and phase relaxation (pure dephasing). The pure dephasing component of Γ_{nm} in general arises from environmentally-induced fluctuations in the energies of each level.[15] When the vibrations are completely uncoupled, e.g. on different molecules where the use of a common ground state is not physically meaningful, these fluctuations must be completely uncorrelated so that the coherence pathway cannot survive the equilibrium average of Eq. 12(b)-(d) and will not contribute to the signal. The presence of coherence in a measurement is therefore a marker of coupling between the vibrations, although the coherent signature is not directly sensitive to the strength of the coupling. Conversely, as we will discuss in Section IV, in some cases coupled vibrations can fail to produce a coherence due to their transition dipoles' orientational configuration within the molecule.

3. Coherence magnitude and sign

The product of the four unique transition dipole moments in a coherence pathway is always real, owing to the closed loop form of the ladder diagrams (Fig. 4(a)).[51] Alternatively, the individual dipole matrix elements may simply be taken to be real by invoking time-reversal symmetry arguments.[51,58] In either case, the amplitudes of the matched pathways in a coherence pair are therefore identical. Explicitly, the Condon approximation amplitude is

$$\begin{aligned} M^*_{en}M_{em}M^*_{n0}M_{m0} &= M^*_{em}M_{en}M^*_{m0}M_{n0} \\ &= |\mu_{eg}|^2\langle 0^e|1^g_n\rangle\langle 0^e|1^g_m\rangle\mu_{n0}\mu_{m0}. \end{aligned} \tag{25}$$

The transition dipole moments of both vibrations and their respective FC factors contribute to the pathway pair's amplitude. As such, the strength of the coherence can be thought of as being determined by a "mixture" (specifically, the geometric mean) of the two vibrations' FEIR activities. Crucially, the product of these four factors can be positive or negative, contributing an overall sign to the coherence. This sign, if negative, can equivalently be considered as an initial π phase-shift to the coherence cycle, the situation discussed above in Fig. 4 being the case of a positively-signed coherence. Furthermore, as we will discuss in Sec. IV, the orientational response for the coherence

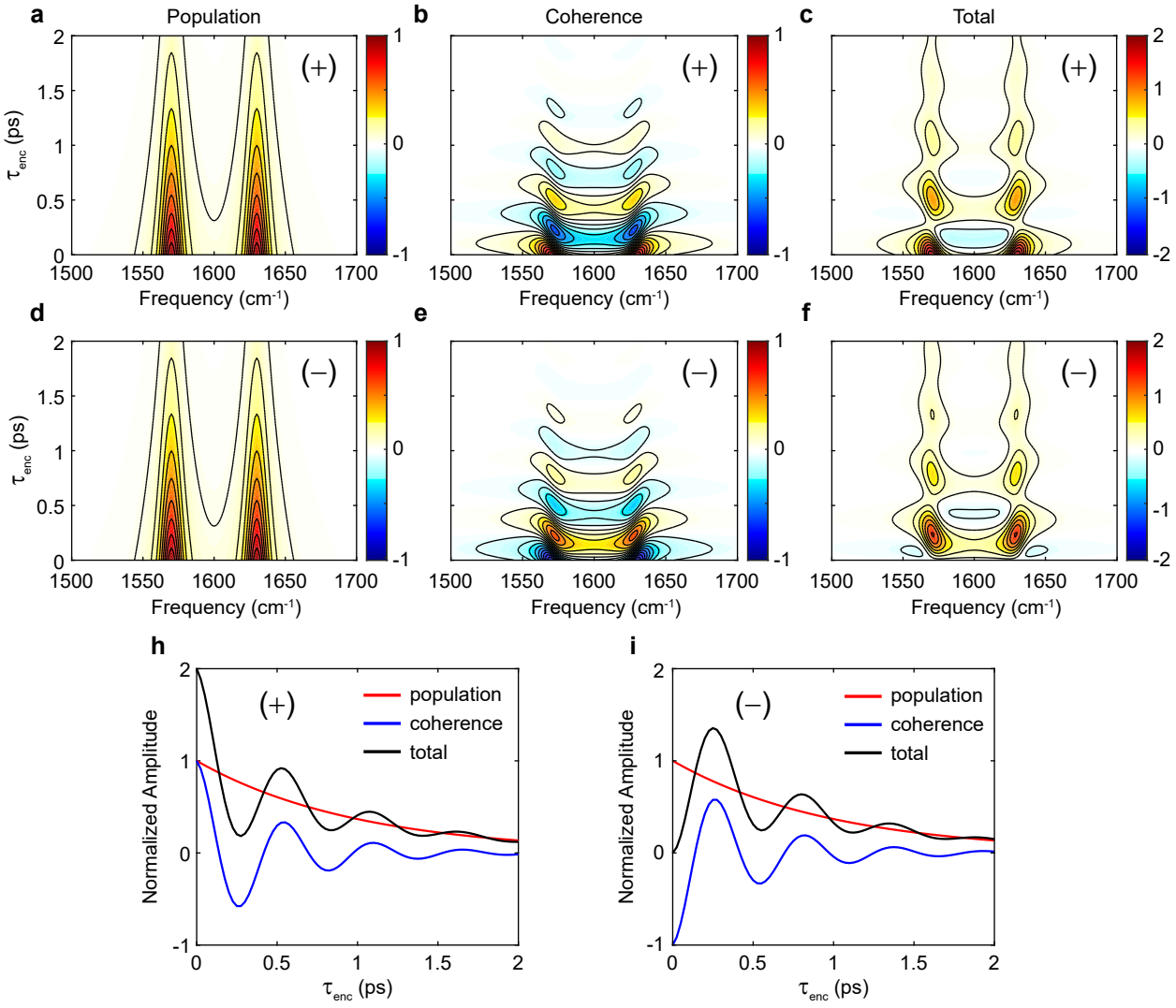

FIG. 5. Interference between population and coherence contributions of positive (+) or negative (-) sign for a system of two coupled modes. Contributions to the impulsive-limit τ_{enc}-dependent FEIR spectrum from (a) population pathways ($C_1^{0,m,e,m} + C_1^{0,n,e,n} + C_2^{0,m,e,m} + C_2^{0,n,e,n} + c.c.$), (b) coherence pathways ($C_1^{0,m,e,n} + C_1^{0,n,e,m} + C_2^{0,m,e,n} + C_2^{0,n,e,m} + c.c.$), and (c) the resulting total spectrum, i.e. the sum over all pathways, in the case of a positively-signed coherence (similarly-signed FC factors). (d)-(f) show the analogous case for a negatively-signed coherence (oppositely-signed FC factors). (h) and (i) show the corresponding two-pulse signal and its population and coherence contributions for the positively- and negatively-signed coherence cases, respectively. In each case, amplitudes are normalized to the maximum of the population response, and population and coherence contributions add up to the total signal.

can additionally influence both its magnitude and sign.

Without loss of generality we take the vibrational matrix elements μ_{m0} and μ_{n0} to be positive, and let their dipole unit vectors in the orientational correlation functions assume any direction. In the Condon approximation the vibronic transitions are aligned along the bare electronic transition dipole unit vector $\hat{\boldsymbol{\mu}}_{eg}$ (Eq. 3). Therefore we set both the vibronic transition dipole unit vectors to be $\hat{\boldsymbol{\mu}}_{eg}$ in the orientational correlation functions, while the FC factors $\langle 0^e|1^g_m\rangle$ and $\langle 0^e|1^g_n\rangle$ can vary in sign. For example, in the displaced harmonic oscillator model $\langle 0^e|1^g_i\rangle = (d_i/\sqrt{2})\exp(-d_i^2/4)$. In this case, the FC factor sign is controlled by the sign of the dimensionless displacement d_i, i.e. whether the relaxed nuclear geometry in the excited state is extended (positive d_i) or contracted (negative d_i) along mode i relative to the ground state. Changes in mode frequency between the ground and excited sates cannot change the FC factor sign, while Duschinksy mixing can in general affect the sign.[45] If both FC factors $\langle 0^e|1^g_m\rangle$ and $\langle 0^e|1^g_n\rangle$ have the same sign, the coherence amplitude (Eq. 25) is positive, while opposite signs consequently lead to a negative coherence amplitude.

D. Interference of population and coherence pathways

The overall sign of the coherence amplitude has dramatic consequences for the way in which population and coherence contributions interfere to produce the total FEIR signal, and are demonstrated in Fig. 5. Panels (a), (b), and (c) show the contribution to the vibronic response of the population pathways, coherence pathways, and both in the two-mode system's τ_{enc}-dependent FEIR spectrum for the case were both FC factors have the same sign, resulting in a positively-signed coherence. At $\tau_{\text{enc}} = 0$ fs the positive absorptive coherence lineshape interferes constructively with the population features, leading to maximally intense, absorptive lineshapes in the spectrum. This constructive interference correspondingly leads to a maximum at $\tau_{\text{enc}} = 0$ fs in the two-pulse signal, shown in Fig. 5(h).

The case of oppositely-signed FC factors resulting in a negatively-signed coherence is shown analogously in Figs. 5(d)-(f) and (i). The population features in panel (d) are unchanged (c.f. panel (a)), as they depend on the squared magnitude of matrix elements (i.e. the vibrations' respective FEIR activities Eq. 19). However, the coherence amplitude is inverted, producing π phase-shifted oscillations relative to panel (b). As a result, the total spectrum is subject to destructive interference between the population and coherence features at $\tau_{\text{enc}} = 0$ fs. In this example the modes have equal

FEIR activities and linewidths, so this destructive interference is complete, as can be seen by the total cancellation of two-pulse signal at $\tau_{\text{enc}} = 0$ fs in Fig. 5(i). Instead, the two-pulse signal is peaked at the first half-cycle of coherence phase evolution near $\tau_{\text{enc}} \sim 250$ fs, where the total spectrum's lineshape is also fully absorptive. We note that the two-pulse signal remains non-negative in all cases, even with unequal FEIR activities (not shown)—a direct consequence of retaining only the correlation functions C_1 and C_2 that, when all material pathways are summed over, contribute positively to $\bar{N}^{(4)}$.

An approach to separating the population and coherence contributions in broadband FEIR signals using a Fourier transform along τ_{enc} was investigated in Ref. 14. Similar to "beating maps" and related Fourier analyses of waiting-time-dependent 2D spectra,[59–63] this method relies on sufficient separation between the frequency content of coherent beating (centered at the vibrational difference frequency $|\omega_{ij}|$ with spread given by the dephasing Γ_{ij}) and population decay (zero-centered with spread determined by the relaxation rate Γ_{ii}). While the isolated population response could in principle be recovered for systems satisfying this condition, the large amount of data required (i.e. a series of spectra properly sampled in τ_{enc}) is incompatible with the limited photon budgets encountered in single-molecule measurements.

IV. ORIENTATIONAL RESPONSE

A. Orientational correlation functions and polarization-dependence of FEIR signals

The orientational contribution to the response function encodes the relative molecular frame orientation of the multiple transitions involved in each pathway and any dynamics that reorient them between successive light-matter interactions. The direct formal correspondence in orientational response between FEIR and third-order coherent techniques—both being described by four-point dipole unit vector correlation functions—leads to useful analogies in the design of polarization-dependent experiments and allows us to adopt similar notation in their theoretical description. Earlier work on picosecond IR-UV/Vis double-resonance fluorescence techniques, which are closely-related precursors of FEIR spectroscopy, investigated the polarization dependence of signals in terms of the relative angle between the vibrational and electronic transitions and its relaxation.[64–66] The more general response function description we employ here allows us to treat orientational effects for both the population and coherent response in multimode FEIR

experiments.

The orientational pathways in Eq. 13 are

$$(Y_1)^{a,b,c,d}_{IJKL}(\tau_3,\tau_2,\tau_1) = \sum_{ijkl} \tilde{T}^{ijkl}_{IJKL}(\tau_3,\tau_2,\tau_1)\left[\hat{\mathbf{m}}_{dc}\cdot\hat{i}\right]\left[\hat{\mathbf{m}}_{cb}\cdot\hat{j}\right]\left[\hat{\mathbf{m}}_{ad}\cdot\hat{k}\right]\left[\hat{\mathbf{m}}_{ba}\cdot\hat{l}\right] \tag{26a}$$

$$(Y_2)^{a,b,c,d}_{IJKL}(\tau_3,\tau_2,\tau_1) = \sum_{ijkl} \tilde{T}^{ijkl}_{IJKL}(\tau_3,\tau_2,\tau_1)\left[\hat{\mathbf{m}}_{cb}\cdot\hat{i}\right]\left[\hat{\mathbf{m}}_{dc}\cdot\hat{j}\right]\left[\hat{\mathbf{m}}_{ad}\cdot\hat{k}\right]\left[\hat{\mathbf{m}}_{ba}\cdot\hat{l}\right] \tag{26b}$$

$$(Y_3)^{a,b,c,d}_{IJKL}(\tau_3,\tau_2,\tau_1) = \sum_{ijkl} \tilde{T}^{ijkl}_{IJKL}(\tau_3,\tau_2,\tau_1)\left[\hat{\mathbf{m}}_{dc}\cdot\hat{i}\right]\left[\hat{\mathbf{m}}_{ad}\cdot\hat{j}\right]\left[\hat{\mathbf{m}}_{cb}\cdot\hat{k}\right]\left[\hat{\mathbf{m}}_{ba}\cdot\hat{l}\right]. \tag{26c}$$

where $\hat{i},\hat{j},\hat{k}$, and $\hat{l}$ are the unit vectors along the Cartesian coordinates x, y, and z in the molecular frame. Here $\tilde{T}^{ijkl}_{IJKL}(\tau_3,\tau_2,\tau_1)$ accounts for orientational dynamics and performs the orientational average to transform the molecular-frame to lab-frame coordinates. As the pathways only differ in the sequential ordering of the four transition dipole unit vectors, we will denote a generic pathway by listing these molecular-frame dipoles as superscripts from right to left in order of interaction, e.g. $Y^{\sigma\rho\nu\mu}_{IJKL}$ represents $(Y_1)^{a,b,c,d}_{IJKL}$ in Eq. 26 when $\boldsymbol{\mu} = \hat{\boldsymbol{\mu}}_{ba}$, $\boldsymbol{\nu} = \hat{\boldsymbol{\mu}}_{ad}$, $\boldsymbol{\rho} = \hat{\boldsymbol{\mu}}_{cb}$, and $\boldsymbol{\sigma} = \hat{\boldsymbol{\mu}}_{dc}$. Alternatively, these superscripts will be suppressed when discussing properties of the orientational tensor common to any set of dipoles.

We will use isotropic rotational averaging consistent with a solution-phase ensemble. In this case, evaluation of the sums in Eq. 26 is simplified by the symmetries of isotropic tensors,[67] reducing the number of terms from $3^4 = 81$ to 21,

$$\begin{aligned} Y^{\sigma\rho\nu\mu}_{IJKL} &= \sum_{ijkl} \tilde{T}^{ijkl}_{IJKL}\sigma_i\rho_j\nu_k\mu_l \\ &= \sum_{i\neq j}\Big[\tilde{T}^{iiii}_{IJKL}\sigma_i\rho_i\nu_i\mu_i + \tilde{T}^{iijj}_{IJKL}\sigma_i\rho_i\nu_j\mu_j \\ &\quad + \tilde{T}^{ijij}_{IJKL}\sigma_i\rho_j\nu_i\mu_j + \tilde{T}^{ijji}_{IJKL}\sigma_i\rho_j\nu_j\mu_i\Big], \end{aligned} \tag{27}$$

where the time-dependence has been suppressed for clarity. Expressions for the nonvanishing elements $\tilde{T}^{ijkl}_{IJKL}(\tau_3,\tau_2,\tau_1)$ derived for the orientational relaxation of a spherical rotor within a classical small-angle rotational diffusion equation are well-established.[43,68,69] In the absence of orientational dynamics, $\tilde{T}^{ijkl}_{IJKL}$ is simply the fourth-rank isotropic tensor that performs the rotational

average, and has a straightforward expression in terms of rotational invariants.[16,70,71] In the context of FEIR experiments, orientational relaxation is largely due to body-fixed rotation of the entire molecule, which for typical fluorophores in solution occurs on the timescale of tens to hundreds of picoseconds or longer[72,73]—usually significantly slower than vibrational dephasing and population relaxation. For simplicity we will therefore leave orientational relaxation out of the notation, although its effects may be readily incorporated by substituting time-dependent versions of the $\tilde{T}^{ijkl}_{IJKL}$ in the expressions.

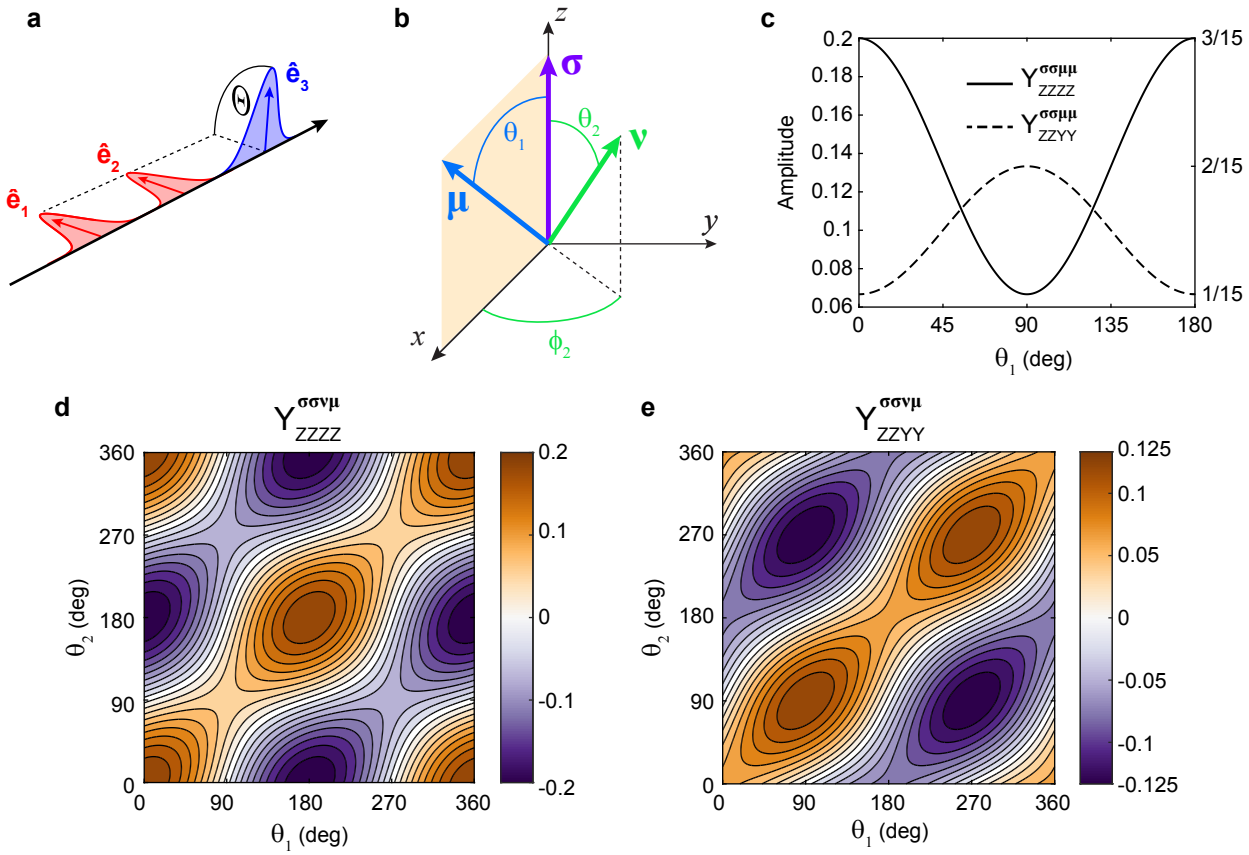

FIG. 6. Polarized FEIR pulse sequence and orientational correlation functions for two (population pathways) and three (coherence pathways) independent transition dipole directions. (a) Pulse sequence indicating the experimental polarization angle Θ. (b) Angular variables describing three arbitrarily oriented dipole unit vectors in the molecular frame. (c) Two-dipole orientational correlation functions $Y^{\sigma\sigma\mu\mu}_{ZZZZ}$ and $Y^{\sigma\sigma\mu\mu}_{ZZYY}$ as a function of the projection angle θ_1 (Eqs. 29(a) and (b)). (d) Three-dipole correlation functions $Y^{\sigma\sigma\nu\mu}_{ZZZZ}$ and (e) $Y^{\sigma\sigma\nu\mu}_{ZZYY}$ in the case of co-planar dipoles (Eqs. 32(a) and (b)).

The polarization geometry of an FEIR experiment is shown in Fig. 6(a), where each pulse's

electric field polarization unit vector is denoted by $\hat{\mathbf{e}}_\alpha$ for $\alpha = 1, 2$, or 3. Both IR pulses $\hat{\mathbf{e}}_1$ and $\hat{\mathbf{e}}_2$ have the same linear polarization, which may be varied by an angle Θ with respect to the linear polarization of the encoding pulse $\hat{\mathbf{e}}_3$. This arrangement is directly analogous to that in polarization-dependent 2D spectroscopy experiments in the pump-probe geometry.[52] Taking the beam's direction of propagation to lie along the lab-frame X axis and $\hat{\mathbf{e}}_3$ along the Z axis, the polarization-dependence of any signal F (neglecting C_3 pathways) is given by the linear combination

$$F(\Theta) \propto (Y_{ZZZZ} - Y_{ZZYY})\cos^2(\Theta) + Y_{ZZYY}. \tag{28}$$

The parallel $F_{ZZZZ} \equiv F(\Theta = 0^\circ)$ and perpendicular $F_{ZZYY} \equiv F(\Theta = 90^\circ)$ signals isolate the respective tensor elements accordingly.

B. Orientational correlation functions for population and coherence pathways

In FEIR spectroscopy the number of unique transitions appearing in any pathway can either be two (for population pathways), or four (for coherence pathways). Population pathways involve one vibrational fundamental, $\boldsymbol{\mu} = \boldsymbol{\nu}$, and one vibronic transition $\boldsymbol{\rho} = \boldsymbol{\sigma}$. In this case the orientational response depends only the projection angle of one dipole onto the other, shown e.g. by θ_1 between $\boldsymbol{\mu}$ and $\boldsymbol{\sigma}$ in Fig. 6(b). This case is common to the 2D spectroscopy of coupled transitions, e.g. the orientational dependence of a cross-peak.[69] Specifically, evaluating Eq. 27 the two-dipole orientational correlation functions are

$$Y_{ZZZZ}^{\boldsymbol{\sigma}\boldsymbol{\sigma}\boldsymbol{\mu}\boldsymbol{\mu}} = \frac{1}{15}\Big(2\cos^2\theta_1 + 1\Big), \tag{29a}$$

$$Y_{ZZYY}^{\boldsymbol{\sigma}\boldsymbol{\sigma}\boldsymbol{\mu}\boldsymbol{\mu}} = \frac{1}{15}\Big(2 - \cos^2\theta_1\Big), \tag{29b}$$

which are plotted in Fig. 6(c).

On the other hand, coherence pathways involve four different transition dipoles, which in the most general case could each have unique orientations in the molecular frame. This most general case therefore has an intrinsic dependence on five angles: one to set the relative orientation of the first two dipoles, then two more for each successive dipole to fully determine its orientation relative to the first two. If all dipoles are co-planar the problem reduces to three angular degrees of freedom.[49] Here we will take the Condon approximation where the vibronic transitions are all parallel to the bare electronic transition (Eq. 3). In this case the number of unique transition

dipole unit vectors in a coherence pathway reduces to three—two ground state vibrational transition dipoles $\boldsymbol{\mu}$ and $\boldsymbol{\nu}$, and the electronic transition dipole $\boldsymbol{\rho} = \boldsymbol{\sigma}$, and in general three angles are required.

Figure 6(b) shows the arrangement of the three unit dipoles in the molecular frame. We take the electronic transition dipole $\boldsymbol{\sigma}$ to be aligned along the z axis. Then without loss of generality, one of the vibrational transition dipoles, $\boldsymbol{\mu}$, can be taken to lie in the xz plane with polar angle θ_1, while the other, $\boldsymbol{\nu}$, is described by the polar and azimuthal angles θ_2 and ϕ_2, respectively. Explicitly, the molecular-frame components of each unit dipole are

$$\boldsymbol{\sigma} = \begin{bmatrix} \sigma_x \\ \sigma_y \\ \sigma_z \end{bmatrix} = \begin{bmatrix} 0 \\ 0 \\ 1 \end{bmatrix}, \quad \boldsymbol{\mu} = \begin{bmatrix} \sin\theta_1 \\ 0 \\ \cos\theta_1 \end{bmatrix}, \quad \boldsymbol{\nu} = \begin{bmatrix} \cos\phi_2 \sin\theta_2 \\ \sin\phi_2 \sin\theta_2 \\ \cos\theta_2 \end{bmatrix}. \tag{30}$$

In the all parallel polarization geometry, we find only two non-vanishing terms in Eq. 27

$$\begin{aligned} Y_{ZZZZ}^{\boldsymbol{\sigma\sigma\nu\mu}} &= \tilde{T}_{ZZZZ}^{zzzz}(\sigma_z)^2 \nu_z \mu_z + \tilde{T}_{ZZZZ}^{zzxx}(\sigma_z)^2 \nu_x \mu_x \\ &= \frac{1}{5}\cos\theta_1 \cos\theta_2 + \frac{1}{15}\cos\phi_2 \sin\theta_1 \sin\theta_2. \end{aligned} \tag{31a}$$

Similarly, for perpendicular polarization we have

$$\begin{aligned} Y_{ZZYY}^{\boldsymbol{\sigma\sigma\nu\mu}} &= \tilde{T}_{ZZYY}^{zzzz}(\sigma_z)^2 \nu_z \mu_z + \tilde{T}_{ZZYY}^{zzxx}(\sigma_z)^2 \nu_x \mu_x \\ &= \frac{1}{15}\cos\theta_1 \cos\theta_2 + \frac{2}{15}\cos\phi_2 \sin\theta_1 \sin\theta_2. \end{aligned} \tag{31b}$$

The fluorophores used in FEIR experiments are electronically-conjugated molecules in which the electronic transition dipole is typically contained in the plane of the conjugated core. The mid-IR vibrations being interrogated most often involve the in-plane motion of the core's nuclei, and therefore also have transition dipoles in this same plane. In this case, all transition dipoles are co-planar, and ϕ_2 can be set to zero. The resulting three-dipole orientational correlation functions in the co-planar limit are

$$\begin{aligned} Y_{ZZZZ}^{\boldsymbol{\sigma\sigma\nu\mu}} &= \frac{1}{5}\cos\theta_1 \cos\theta_2 + \frac{1}{15}\sin\theta_1 \sin\theta_2 \\ &= \frac{1}{15}\Big(2\cos(\theta_1 - \theta_2) + \cos(\theta_1 + \theta_2)\Big), \end{aligned} \tag{32a}$$

$$\begin{aligned} Y_{ZZYY}^{\boldsymbol{\sigma\sigma\nu\mu}} &= \frac{1}{15}\cos\theta_1 \cos\theta_2 + \frac{2}{15}\sin\theta_1 \sin\theta_2 \\ &= \frac{1}{30}\Big(3\cos(\theta_1 - \theta_2) - \cos(\theta_1 + \theta_2)\Big), \end{aligned} \tag{32b}$$

and are plotted in Fig. 6(d) and (e). These expressions can be seen to coincide with those derived for four co-planar dipoles in Ref. 74 by Khalil and coworkers for 2D VE and 2D EV experiments when two of the four become parallel. We note that the three-dipole orientational correlation functions are anti-symmetric with respect to π shifts in either angle, e.g. $Y_{ZZZZ}(\theta_1+\pi,\theta_2) = -Y_{ZZZZ}(\theta_1,\theta_2) = Y_{ZZZZ}(\theta_1,\theta_2+\pi)$. When $\boldsymbol{\mu}=\boldsymbol{\nu}$, only a single projection angle $\theta_1=\theta_2$ is at play, and these expressions reduce to the two-dipole orientational correlation functions in Eq. 29.

Unlike the more commonly encountered two-dipole orientational terms, the three-dipole terms can achieve either positive or negative values, which has important consequences for how coherences manifest in FEIR signals. Specifically, the coherence's sign, and consequently whether constructive or destructive interference with the population pathways occurs at early times, can be influenced by the orientational contribution. For example, two modes which have oppositely signed $\langle 0^e|1^g\rangle$ FC overlaps and therefore produce a negatively-signed coherence in the vibronic response could in fact contribute a positively-signed coherence due to a negative orientational response. Furthermore, the variable sign produces zero-crossings where the orientational response vanishes. Specifically, the locus of zero-crossings indicated by the white contours in Figs. 6(d) and (e) indicate molecular-frame dipole orientations where coherences cannot occur in one polarization geometry or the other. These curves intersect at angle-pair locations that correspond to one vibrational dipole aligned parallel to the electronic transition and the other perpendicular to it. This molecular configuration cannot produce a coherence in any polarization geometry. Similarly, coherences with vibrational transition dipoles falling in regions of the (θ_1,θ_2) plane where Y_{ZZZZ} and Y_{ZZYY} have opposite sign, i.e. that are bounded between their zero-crossing curves, can be made to vanish with an appropriate choice of polarization angle Θ.

C. Polarization anisotropy

In analogy to its use in third-order spectroscopies,[16,69,75–79] the polarization anisotropy r of the FEIR signal may be defined as

$$r = \frac{F_{ZZZZ} - F_{ZZYY}}{F_{ZZZZ} + 2F_{ZZYY}}. \tag{33}$$

The anisotropy is especially useful when the orientational response is due to two-dipole terms, i.e. when the isolated population response can be measured. Specifically, in a single-mode system without any orientational dynamics the anisotropy has the well-known second Legendre polyno-

mial form

$$r = \frac{1}{5}\Big(3\cos^2\theta - 1\Big), \tag{34}$$

where θ is the projection angle between the vibrational and electronic (or in the more general non-Condon case, vibronic) transition dipole unit vectors. This expression can be used to extract the projection angle up to the degeneracy between θ and $\pi - \theta$, and can be applied individually to well-resolved bands in an FEIR spectrum if coherence contributions are negligibly small or have dephased. As coherence pathways have more complicated three-dipole orientational dependencies described by Eqs. 31 or 32, their contribution to the anisotropy is likely too complex for practical experimental utility.

In the case of orientational motion due to body-fixed rotation of the molecule, the population response anisotropy decay is independent of population dynamics and can be used as a probe of orientational dynamics. The opposite effect, i.e. removing the orientational contribution to the signal, may be accomplished by recording the isotropic component of the FEIR signal

$$F_{\text{iso}} = \frac{1}{3}(F_{ZZZZ} + 2F_{ZZYY}), \tag{35}$$

i.e. from the denominator in Eq. 33. This isotropic component may equivalently be measured directly using magic angle polarization $\Theta = \arctan(\sqrt{2}) \approx 54.7^\circ$.

V. CONCLUSIONS

In this work we have presented a theoretical framework for describing FEIR spectroscopy experiments based on a fourth-order action response function, and developed homogeneous-limit expressions for the vibronic and orientational response relevant for a two-level electronic system coupled to multiple vibrations in the Condon approximation. The restrictions posed by the resonance conditions and system level structure select a relatively small number of pathways that can contribute to the molecular response, consistent with the physical picture of a sequential double-resonance excitation process. These pathways are differentiated in whether they exist in an excited vibrational population or a coherence between vibrational excited states during the encoding delay. The population pathways produce intuitive spectroscopic features that are desirable for measuring one-dimensional spectra, for example in applications of FEIR spectroscopy for highly-sensitive or single-molecule vibrational detection. The coherence pathways complicate this situation by pro-

ducing phase-modulated lineshapes that can interfere with the population features in complex and often non-intuitive ways, especially owing to their variable sign.

The polarization dependence of population features is controlled by orientational correlation functions involving the vibrational and electronic transition dipole unit vectors, and can be used to extract their relative projection angle, e.g. via the polarization anisotropy. This spectroscopic information is useful in a number of ways, as accessing the relative orientation of multiple transitions in a molecule provides further insight into its structure, while also helping to assign the features of complicated spectra. From a detection sensitivity standpoint, polarization dependence could be a useful control parameter to maximize signal brightness from a given vibration or suppress that of another. Coherence pathways bear more complex orientational dependencies that may complicate the extraction of projection angles from polarization-dependent experiments. However, the variable sign of these orientational factors indicate that in some cases coherences can be suppressed or removed entirely by controlling polarization.

While the presence of vibrational coherence can represent a complicating factor in FEIR measurements, it also offers potentially useful molecular information not contained in the population response. Besides indicating that vibrations are coupled within a molecule, which could be used to differentiate a mixture of distinct chemical species, the sensitivity of coherence to the relative sign of the vibrations' FC factors could in principle be of interest. These signs, which are typically not measurable in vibronic spectroscopies, provide a more detailed geometric view of vibronic coupling in the molecule. For example, in the displaced harmonic oscillator model the sign of $\langle 0^e | 1_i^g \rangle$ reflects the sign of the displacement between the ground and electronic states along the vibrational coordinate. Overall, the ability to extract useful information from FEIR observables and achieve high detection sensitivity are deeply related and highly dependent on experimental design. Paper II of this series explores how the spectroscopic features presented here appear in experimental data, and discusses how these data can be interpreted.

ACKNOWLEDGEMENTS

This work was supported by a grant from the National Science Foundation (CHE-2155027). We thank Seung Yeon Lee for helpful comments on the manuscript.

AUTHOR DECLARATIONS

Conflict of interest

The authors have no conflicts to disclose.

Author contributions

Lukas Whaley-Mayda: Conceptualization (equal); Methodology (lead); Formal analysis (lead); Visualization (lead); Writing - original draft preparation (lead). Writing - review and editing (equal). **Abhirup Guha**: Methodology (supporting); Formal analysis (supporting); Writing - review and editing (equal). **Andrei Tokmakoff**: Conceptualization (equal); Funding acquisition (lead); Supervision (lead), Writing - review and editing (equal).

DATA AVAILABILITY

The data that support the findings of this study are available from the corresponding author upon reasonable request.

REFERENCES

[1]K. Kneipp, Y. Wang, H. Kneipp, L. T. Perelman, I. Itzkan, R. R. Dasari, and M. S. Feld, "Single molecule detection using surface-enhanced Raman scattering (SERS)," Phys. Rev. Lett. **78**, 1667–1670 (1997).

[2]S. Nie and S. R. Emory, "Probing single molecules and single nanoparticles by surface-enhanced Raman scattering," Science **275**, 1102–1106 (1997).

[3]Y. Yu, T.-H. Xiao, Y. Wu, W. Li, Q.-G. Zeng, L. Long, and Z.-Y. Li, "Roadmap for single-molecule surface-enhanced Raman spectroscopy," Adv. Photonics **2**, 1 – 20 (2020).

[4]F. S. Ruggeri, B. Mannini, R. Schmid, M. Vendruscolo, and T. P. J. Knowles, "Single molecule secondary structure determination of proteins through infrared absorption nanospectroscopy," Nat. Commun. **11**, 1–9 (2020).

[5]B. Choi, G. Jeong, H.-H. Shin, and Z. H. Kim, "Molecular vibrational imaging at nanoscale," J. Chem. Phys. **156**, 160902 (2022).

[6]H. Xiong, L. Shi, L. Wei, Y. Shen, R. Long, Z. Zhao, and W. Min, "Stimulated Raman excited fluorescence spectroscopy and imaging," Nat. Photonics **13**, 412–417 (2019).

[7]R. Chikkaraddy, R. Arul, L. A. Jakob, and J. J. Baumberg, "Single-molecule mid-infrared spectroscopy and detection through vibrationally assisted luminescence," Nat. Photonics **17**, 865–871 (2023).

[8]E. C. Le Ru and P. G. Etchegoin, "Single-molecule surface-enhanced Raman spectroscopy," Annu. Rev. Phys. Chem. **63**, 65–87 (2012).

[9]A. B. Zrimsek, N. Chiang, M. Mattei, S. Zaleski, M. O. McAnally, C. T. Chapman, A.-I. Henry, G. C. Schatz, and R. P. Van Duyne, "Single-molecule chemistry with surface- and tip-enhanced Raman spectroscopy," Chem. Rev. **117**, 7583–7613 (2017).

[10]L. Whaley-Mayda, A. Guha, S. B. Penwell, and A. Tokmakoff, "Fluorescence-encoded infrared vibrational spectroscopy with single-molecule sensitivity," J. Am. Chem. Soc. **143**, 56 (2021).

[11]L. Whaley-Mayda, S. B. Penwell, and A. Tokmakoff, "Fluorescence-encoded infrared spectroscopy: Ultrafast vibrational spectroscopy on small ensembles of molecules in solution," J. Phys. Chem. Lett. **10**, 1967–1972 (2019).

[12]L. Whaley-Mayda, A. Guha, and A. Tokmakoff, "Resonance conditions, detection quality, and single-molecule sensitivity in fluorescence-encoded infrared vibrational spectroscopy," J. Chem. Phys. **156**, 174202 (2022).

[13]J. N. Mastron and A. Tokmakoff, "Two-photon-excited fluorescence-encoded infrared spectroscopy," J. Phys. Chem. A **120**, 9178–9187 (2016).

[14]J. N. Mastron and A. Tokmakoff, "Fourier transform fluorescence-encoded infrared spectroscopy," J. Phys. Chem. A **122**, 554–562 (2018).

[15]S. Mukamel, *Principles of Nonlinear Optical Spectroscopy* (Oxford University Press, New York, 1995).

[16]M. Cho, *Two-Dimensional Optical Spectroscopy* (CRC Press, 2009).

[17]P. Tian, D. Keusters, Y. Suzaki, and W. S. Warren, "Femtosecond phase-coherent two-dimensional spectroscopy," Science **300**, 1553–1555 (2003).

[18]P. F. Tekavec, G. A. Lott, and A. H. Marcus, "Fluorescence-detected two-dimensional electronic coherence spectroscopy by acousto-optic phase modulation," J. Chem. Phys. **127**, 214307 (2007).

[19]A. K. De, D. Monahan, J. M. Dawlaty, and G. R. Fleming, "Two-dimensional fluorescence-detected coherent spectroscopy with absolute phasing by confocal imaging of a dynamic grating

and 27-step phase-cycling," J. Chem. Phys. **140**, 194201 (2014).

[20]S. Draeger, S. Roeding, and T. Brixner, "Rapid-scan coherent 2D fluorescence spectroscopy," Opt. Express **25**, 3259–3267 (2017).

[21]V. Tiwari, Y. A. Matutes, A. T. Gardiner, T. L. Jansen, R. J. Cogdell, and J. P. Ogilvie, "Spatially-resolved fluorescence-detected two-dimensional electronic spectroscopy probes varying excitonic structure in photosynthetic bacteria," Nat. Commun. **9**, 1–10 (2018).

[22]G. Nardin, T. M. Autry, K. L. Silverman, and S. T. Cundiff, "Multidimensional coherent photocurrent spectroscopy of a semiconductor nanostructure," Opt. Express **21**, 28617–28627 (2013).

[23]K. J. Karki, J. R. Widom, J. Seibt, I. Moody, M. C. Lonergan, T. Pullerits, and A. H. Marcus, "Coherent two-dimensional photocurrent spectroscopy in a PbS quantum dot photocell," Nat. Commun. **5** (2014).

[24]A. A. Bakulin, C. Silva, and E. Vella, "Ultrafast spectroscopy with photocurrent detection: Watching excitonic optoelectronic systems at work," J. Phys. Chem. Lett. **7**, 250–258 (2016).

[25]P. Grégoire, A. R. Srimath Kandada, E. Vella, C. Tao, R. Leonelli, and C. Silva, "Incoherent population mixing contributions to phase-modulation two-dimensional coherent excitation spectra," J. Chem. Phys. **147**, 114201 (2017).

[26]N. Zhou, Z. Ouyang, J. Hu, O. F. Williams, L. Yan, W. You, and A. M. Moran, "Distinguishing energy- and charge-transfer processes in layered perovskite quantum wells with two-dimensional action spectroscopies," J. Phys. Chem. Lett. **11**, 4570–4577 (2020).

[27]L. Bolzonello, F. Bernal-Texca, L. G. Gerling, J. Ockova, E. Collini, J. Martorell, and N. F. van Hulst, "Photocurrent-detected 2D electronic spectroscopy reveals ultrafast hole transfer in operating PM6/Y6 organic solar cells," J. Phys. Chem. Lett. **12**, 3983–3988 (2021).

[28]M. Aeschlimann, T. Brixner, A. Fischer, C. Kramer, P. Melchior, W. Pfeiffer, C. Schneider, C. Strüber, P. Tuchscherer, and D. V. Voronine, "Coherent two-dimensional nanoscopy," Science **333**, 1723–1726 (2011).

[29]S. Roeding and T. Brixner, "Coherent two-dimensional electronic mass spectrometry," Nat. Commun. **9** (2018).

[30]L. Bruder, U. Bangert, M. Binz, D. Uhl, R. Vexiau, N. Bouloufa-Maafa, O. Dulieu, and F. Stienkemeier, "Coherent multidimensional spectroscopy of dilute gas-phase nanosystems," Nat. Commun. **9** (2018).

[31]L. Bruder, U. Bangert, M. Binz, D. Uhl, and F. Stienkemeier, "Coherent multidimensional spectroscopy in the gas phase," J. Phys. B: At. Mol. Opt. Phys. **52**, 183501 (2019).

[32]L. Chen, Z. Ma, and J. A. Fournier, "Ultrafast transient vibrational action spectroscopy of cryogenically cooled ions," J. Chem. Phys. **159**, 041101 (2023).

[33]A. Perdomo-Ortiz, J. R. Widom, G. A. Lott, A. Aspuru-Guzik, and A. H. Marcus, "Conformation and electronic population transfer in membrane-supported self-assembled porphyrin dimers by 2D fluorescence spectroscopy," J. Phys. Chem. B **116**, 10757–10770 (2012).

[34]M. Schröter, T. Pullerits, and O. Kühn, "Using fluorescence detected two-dimensional spectroscopy to investigate initial exciton delocalization between coupled chromophores," J. Chem. Phys. **149**, 114107 (2018).

[35]O. Kühn, T. Mančal, and T. Pullerits, "Interpreting fluorescence detected two-dimensional electronic spectroscopy," J. Phys. Chem. Lett. **11**, 838–842 (2020).

[36]P. Malý, S. Mueller, J. Lüttig, C. Lambert, and T. Brixner, "Signatures of exciton dynamics and interaction in coherently and fluorescence-detected four- and six-wave-mixing two-dimensional electronic spectroscopy," J. Chem. Phys. **153**, 144204 (2020).

[37]V. Tiwari, "Multidimensional electronic spectroscopy in high-definition—combining spectral, temporal, and spatial resolutions," J. Chem. Phys. **154**, 230901 (2021).

[38]T. L. Courtney, Z. W. Fox, K. M. Slenkamp, and M. Khalil, "Two-dimensional vibrational-electronic spectroscopy," J. Chem. Phys. **143**, 154201 (2015).

[39]T. L. Courtney, Z. W. Fox, L. Estergreen, and M. Khalil, "Measuring coherently coupled intramolecular vibrational and charge-transfer dynamics with two-dimensional vibrational–electronic spectroscopy," J. Phys. Chem. Lett. **6**, 1286–1292 (2015).

[40]J. D. Gaynor and M. Khalil, "Signatures of vibronic coupling in two-dimensional electronic-vibrational and vibrational-electronic spectroscopies," J. Chem. Phys. **147**, 094202 (2017).

[41]L. J. G. W. van Wilderen, A. T. Messmer, and J. Bredenbeck, "Mixed IR/Vis two-dimensional spectroscopy: Chemical exchange beyond the vibrational lifetime and sub-ensemble selective photochemistry," Angew. Chem. Int. Ed. **53**, 2667–2672 (2014).

[42]J. von Cosel, J. Cerezo, D. Kern-Michler, C. Neumann, L. J. G. W. van Wilderen, J. Bredenbeck, F. Santoro, and I. Burghardt, "Vibrationally resolved electronic spectra including vibrational pre-excitation: Theory and application to VIPER spectroscopy," J. Chem. Phys. **147**, 164116 (2017).

[43]A. Tokmakoff, "Orientational correlation functions and polarization selectivity for nonlinear spectroscopy of isotropic media. I. Third order," J. Chem. Phys. **105**, 1–12 (1996).

[44]A. C. Albrecht, "Polarizations and assignments of transitions: The method of photoselection," J. Mol. Spectrosc. **6**, 84–108 (1961).

[45]L. Whaley-Mayda, *Fluorescence-Encoded Infrared Spectroscopy for Single-Molecule Vibrational Investigation in Solution*, Ph.D. thesis, University of Chicago (2022).

[46]M. G. Raymer, A. H. Marcus, J. R. Widom, and D. L. P. Vitullo, "Entangled photon-pair two-dimensional fluorescence spectroscopy (EPP-2DFS)," J. Phys. Chem. B **117**, 15559–15575 (2013).

[47]M. G. Raymer, T. Landes, and A. H. Marcus, "Entangled two-photon absorption by atoms and molecules: A quantum optics tutorial," J. Chem. Phys. **155**, 081501 (2021).

[48]M. Cho, G. R. Fleming, and S. Mukamel, "Nonlinear response functions for birefringence and dichroism measurements in condensed phases," J. Chem. Phys. **98**, 5314–5326 (1993).

[49]M. Khalil, N. Demirdöven, and A. Tokmakoff, "Coherent 2D IR spectroscopy: Molecular structure and dynamics in solution," J. Phys. Chem. A **107**, 5258–5279 (2003).

[50]S. M. Gallagher Faeder and D. M. Jonas, "Two-dimensional electronic correlation and relaxation spectra: Theory and model calculations," J. Phys. Chem. A **103**, 10489–10505 (1999).

[51]S. M. Gallagher Faeder and D. M. Jonas, "Phase-resolved time-domain nonlinear optical signals," Phys. Rev. A **62**, 033820 (2000).

[52]L. P. DeFlores, R. A. Nicodemus, and A. Tokmakoff, "Two-dimensional Fourier transform spectroscopy in the pump-probe geometry," Opt. Lett. **32**, 2966–2968 (2007).

[53]S.-H. Shim and M. T. Zanni, "How to turn your pump–probe instrument into a multidimensional spectrometer: 2D IR and Vis spectroscopies via pulse shaping," Phys. Chem. Chem. Phys. **11**, 748–761 (2009).

[54]W. S. Struve, *Fundamentals of Molecular Spectroscopy* (Wiley New York, 1989).

[55]S. Kundu, P. P. Roy, G. R. Fleming, and N. Makri, "Franck–Condon and Herzberg–Teller signatures in molecular absorption and emission spectra," J. Phys. Chem. B **126**, 2899–2911 (2022).

[56]H. Dong, N. H. C. Lewis, T. A. A. Oliver, and G. R. Fleming, "Determining the static electronic and vibrational energy correlations via two-dimensional electronic-vibrational spectroscopy," J. Chem. Phys. **142**, 174201 (2015).

[57]T. Mančal, A. Nemeth, F. Milota, V. Lukeš, H. F. Kauffmann, and J. Sperling, "Vibrational wave packet induced oscillations in two-dimensional electronic spectra. II. Theory," J. Chem. Phys.

132 (2010).

[58]J. J. Sakurai, *Modern Quantum Mechanics; rev. ed.* (Addison-Wesley, Reading, MA, 1994).

[59]D. B. Turner, K. W. Stone, K. Gundogdu, and K. A. Nelson, "Three-dimensional electronic spectroscopy of excitons in GaAs quantum wells," J. Chem. Phys. **131**, 144510 (2009).

[60]T. R. Calhoun, N. S. Ginsberg, G. S. Schlau-Cohen, Y.-C. Cheng, M. Ballottari, R. Bassi, and G. R. Fleming, "Quantum coherence enabled determination of the energy landscape in light-harvesting complex II," J. Phys. Chem. B **113**, 16291–16295 (2009).

[61]F. Milota, V. I. Prokhorenko, T. Mancal, H. von Berlepsch, O. Bixner, H. F. Kauffmann, and J. Hauer, "Vibronic and vibrational coherences in two-dimensional electronic spectra of supramolecular j-aggregates," J. Phys. Chem. A **117**, 6007–6014 (2013).

[62]V. Butkus, D. Zigmantas, D. Abramavicius, and L. Valkunas, "Distinctive character of electronic and vibrational coherences in disordered molecular aggregates," Chem. Phys. Lett. **587**, 93–98 (2013).

[63]A. Volpato, L. Bolzonello, E. Meneghin, and E. Collini, "Global analysis of coherence and population dynamics in 2D electronic spectroscopy," Opt. Express **24**, 24773–24785 (2016).

[64]M. Lettenberger, F. Emmerling, N. Gottfried, and A. Laubereau, "Orientational motion of anthracene in liquid solution studied by IR/UV double-resonance spectroscopy," Chem. Phys. Lett. **240**, 324–329 (1995).

[65]F. Emmerling, M. Lettenberger, and A. Laubereau, "Vibrational dynamics of anthracene in liquid solution studied by picosecond IR/UV spectroscopy with polarization resolution," J. Chem. Phys. **100**, 19251–19256 (1996).

[66]T. Dahinten, J. Baier, and A. Seilmeier, "Vibrational energy transfer processes in dye molecules after ultrafast excitation of skeletal modes," Chem. Phys. **232**, 239–245 (1998).

[67]P. N. Butcher and D. Cotter, *The Elements of Nonlinear Optics*, 9 (Cambridge university press, 1990).

[68]B. J. Berne and R. Pecora, *Dynamic Light Scattering: with Applications to Chemistry, Biology, and Physics* (Courier Corporation, 2000).

[69]O. Golonzka and A. Tokmakoff, "Polarization-selective third-order spectroscopy of coupled vibronic states," J. Chem. Phys. **115**, 297–309 (2001).

[70]D. L. Andrews and T. Thirunamachandran, "On three-dimensional rotational averages," J. Chem. Phys. **67**, 5026–5033 (1977).

[71]R. M. Hochstrasser, "Two-dimensional IR-spectroscopy: polarization anisotropy effects," Chem. Phys. **266**, 273–284 (2001).

[72]M.-L. Horng, J. A. Gardecki, and M. Maroncelli, "Rotational dynamics of coumarin 153: time-dependent friction, dielectric friction, and other nonhydrodynamic effects," J. Phys. Chem. A **101**, 1030–1047 (1997).

[73]G. B. Dutt and S. Raman, "Rotational dynamics of coumarins: An experimental test of dielectric friction theories," J. Chem. Phys. **114**, 6702–6713 (2001).

[74]J. D. Gaynor, R. B. Weakly, and M. Khalil, "Multimode two-dimensional vibronic spectroscopy. I. Orientational response and polarization-selectivity," J. Chem. Phys. **154**, 184201 (2021).

[75]G. Fleming, *Chemical applications of ultrafast spectroscopy* (Oxford University Press, New York, NY, 1986).

[76]D. M. Jonas, M. J. Lang, Y. Nagasawa, T. Joo, and G. R. Fleming, "Pump-probe polarization anisotropy study of femtosecond energy transfer within the photosynthetic reaction center of Rhodobacter sphaeroides R26," J. Phys. Chem. **100**, 12660–12673 (1996).

[77]K. J. Gaffney, I. R. Piletic, and M. D. Fayer, "Orientational relaxation and vibrational excitation transfer in methanol–carbon tetrachloride solutions," J. Chem. Phys. **118**, 2270–2278 (2003).

[78]P. Hamm and M. Zanni, *Concepts and Methods of 2D Infrared Spectroscopy* (Cambridge University Press, 2011).

[79]S. Schott, A. Steinbacher, J. Buback, P. Nuernberger, and T. Brixner, "Generalized magic angle for time-resolved spectroscopy with laser pulses of arbitrary ellipticity," J. Phys. B: At. Mol. Opt. Phy **47**, 124014 (2014).